Constraining the Source Craters of Unbrecciated Lunar Mare Basalt Meteorites

by

Tatiana Mijajlovic

A thesis submitted in partial fulfillment of the requirements for the degree of

Master of Science

Department of Earth and Atmospheric Sciences
University of Alberta

Abstract

MIL 05035, NWA 10597, NWA 8632, NWA 479 and NWA 4898 are all unbrecciated lunar mare basalt meteorites, interpreted to have individually experienced a single hypervelocity collision event that would have resulted in their ejection from the Moon. A comprehensive study of shock deformation and transformation effects constrain the upper and lower boundary limits of bulk shock pressures that would have been experienced during the ejection of each sample. Micro-Raman spectroscopy, electron imaging and optical properties were used characterize the structural state of calcic plagioclase (An_{80-90}) within the meteorites, shock deformation and transformation in pyroxene and olivine, and the mineralogy and microtextures of shock melt within the samples. Confirmation of the partial or total amorphization of plagioclase feldspar to maskelynite constrains lower boundary ranges of 22 – 24 GPa for NWA 10597, 24 – 26 GPa for NWA 4898, and 25 – 27 GPa for MIL 05035, NWA 8632, and NWA 479. These pressures are associated with post-shock temperature increases < 200˚C. The shock deformation of olivine phenocrysts in the form of irregular fractures, weak mosaicism and planar fractures, accompanied by undulose extinction to weak mosaicism, and polysynthetic mechanical twinning of pyroxene phenocrysts constrain the upper limit of the shock pressure to 30 GPa for all five samples. High-pressure mineral investigations within the shock melt of the meteorites combined with Finite Element Heat Transfer (FEHT) modelling of cooling times provides constraints on the pressure-temperature-time history of each sample. This information then points the way for further determining the decay rate of the shock wave each sample experienced, the degree of adiabatic cooling involved in the post-shock environment and modelling the potential source crater diameters. These crater diameters in turn could be used as a potential parameter for constraining the geological unit from which these meteorites originated on the lunar surface.

Preface

The methodology for this study was based on the process followed during an undergraduate thesis supervised by Dr. Erin Walton at MacEwan University, that was then adapted for multiple samples and further developed. The results were then used in Chapter 3 to incorporate thermal modelling and source terrane linking. The literature review in Chapter 1, observations and analyses in Chapter 2, and thermal modelling and final conclusions in Chapter 3 are all my own original work. The incorporation of NWA 032 into the thermal modelling component of Chapter 3 was based on the previous work published as Mijajlovic T., Xie X. and Walton E. L. 2020. A revised shock history for the youngest unbrecciated lunar basalt—Northwest Africa 032 and paired meteorites. *Meteoritics & Planetary Science* 55: 2267–2286; a paper written based on the aforementioned undergraduate thesis.

Acknowledgements

Dedication

This thesis is dedicated to Dr. Erin L. Walton (1978 – 2022) as without her encouragement, support, and guidance there would have been no project. Erin recognized my passion for all things rocks and space during my undergraduate degree and set out to mentor me in the field of planetary geology. It was through her supervision of my undergraduate thesis that I was able to publish my first academic paper. Her support then continued beyond my Bachelor of Science as she stepped forward to co-supervise this very thesis, allowing me to pursue a graduate degree. Everything during my academic career thus far is because Erin was pushing for me, and whatever success I have in the future will be a direct result of Erin investing her time in my hopes and dreams.

Table of Contents

List of Tables

List of Figures

Chapter One

Introduction

Lunar History

   The leading hypothesis of lunar formation suggests that approximately 4.5 billion years ago a collision between a protoplanet and the proto-Earth resulted in the formation of the Moon. The differentiation processes following the collision resulted in a dense, iron-rich core, and a Mg-Fe rich global magma ocean. During the solidification of the magma ocean, buoyant plagioclase would have floated to the top of the convecting magma creating the Ca- and Al-rich crust of the lunar surface. Denser olivine and pyroxene crystals sank to the bottom of the magma forming a cumulate pile. Today, the completely solidified lunar magma ocean contains these cumulates which have overturned in response to gravitational instabilities. The last dregs of the magma ocean became enriched in TiO_2 leading to ilmenite ($FeTiO_3$) and spinel (Fe_2TiO_4) crystallization. During the formation of the lunar crust, intrusive magmatic activity formed a secondary crust that resulted in the magnesian and high-alkali suites of the lunar highlands. The global magma ocean lasted for 150 – 200 Myr. Partial melting lead to the first of the mare basalts at approximately 4.3 Ga according to isotopic dating of mare basalt clasts in lunar meteorites (i.e., Kalahari 009; Warren and Taylor 2014). This era of the Moon's geologic history is known as the pre-Nectarian and lasted until 3.920 Ga (Stöffler et al. 2006). It was during this period that the late-heavy bombardment, also known as the lunar cataclysm, is hypothesized, resurfacing the lunar crust and forming some of the oldest impact basins on the lunar surface (Joy and Arai 2013). Stöffler et al. (2006) provides an excellent review of the Moon's geochronology, which will be summarized here. The geologic timescale of the Moon is divided into six epochs, all characterized by different geologic processes and marked by the creation of prominent impact basins. The first of these epochs, the Pre-Nectarian, refers to landforms older than the Nectaris basin. No volcanic landforms or tectonic features have been found from this period; however, it was dominated by magmatic, thermal metamorphic, and impact geologic processes. It was during the pre-Nectarian that the Oceanus Procellarum and the South Pole Aitken basin were formed (4.2 – 4.1 Ga; Stöffler et al. 2006). Following the pre-Nectarian is the Nectarian epoch, which lasted until 3.850 Ga and is characterized by mare volcanism. Despite the wide range of lunar mare ages provided by the Apollo samples (2.8-4.3 Ga; Warren and Taylor 2014), crater size-frequency distribution suggests most mare basalts erupted between 3.6 and 3.8 Ga with eruptions younger than 2.6 Ga occurring intermittently (Hiesinger et al. 2000). From the Nectarian to the Late

1

Imbrium epoch volcanism dominates the Moon; however, crater counting statistics also suggest that there may be some mare lava flows as young as 1.3 Ga, placing such flows firmly in the Eratosthenian age (Hiesinger et al. 2003). The Early Imbrium is marked by the formation of the Imbrium impact basin until the formation of the Orientale basin (3.850 – 3.750 Ga) with the Late Imbrium spanning until 3.2 Ga. The Apollo missions sampled primarily Late Imbrium mare plains which were formed due to infilling of the pre-existing basins. This is supported by the significant lack of basin deposits formed during this time. Instead, there is an increase in volcanic activity in the Late Imbrium, evidenced by the volcanic glass the Apollo missions found within the maria (Stöffler et al. 2006). The final two epochs of lunar history are the Eratosthenian age (3.2 – 0.8 Ga) and Copernican age (0.8 – present day). The most marked difference between the two epochs is the presence of rayed (Copernican) and non-rayed (Eratosthenian) craters. Following the Eratosthenian epoch, the main geologic processes on the Moon are impacts, with Copernican-aged craters superposed on the other established terrains of the lunar surface (Joy and Arai 2013).

Current Lunar Sample Inventory

Crewed and uncrewed missions to the Moon returned approximately 382 kg of lunar rock and soil to Earth during the space race (Vaniman et al. 1991). The Apollo and Luna missions only sampled 4.4% of the lunar surface (Warren and Kallemeyn 1991) with Apollo landing within the central nearside face of the moon, and Luna exploring the eastern nearside limb (Joy and Arai 2013); both areas occur within or near to the Procellarum KREEP Terrane described in *Composition of Lunar Material* below (Fig. 1). Apollo and Luna samples therefore represent a biased sample suite. In contrast, lunar meteorites are derived from random sampling of the surface via natural hypervelocity impact events, resulting in a sampling of lunar material not collected by the Apollo and Luna missions. The inclusion of lunar meteorites in our terrestrial inventory has increased the amount of material available to study by ~240% of what was returned by Apollo and Luna (https://meteorites.wustl.edu/lunar/Moon_meteorites_list_alpha.htm).

Lunar meteorites are relatively rare, with 554 approved meteorites, representing some 158 distinct lithologies at the time of writing (https://meteorites.wustl.edu/lunar/Moon_meteorites_list_alpha.htm). The difference in approved meteorites and distinct lithologies derives from the launch pairing of lunar meteorites. Launched paired meteorites are believed to have been ejected from the same crater during a single impact event and can also be referred to as source-crater paired (Korotev 2005).
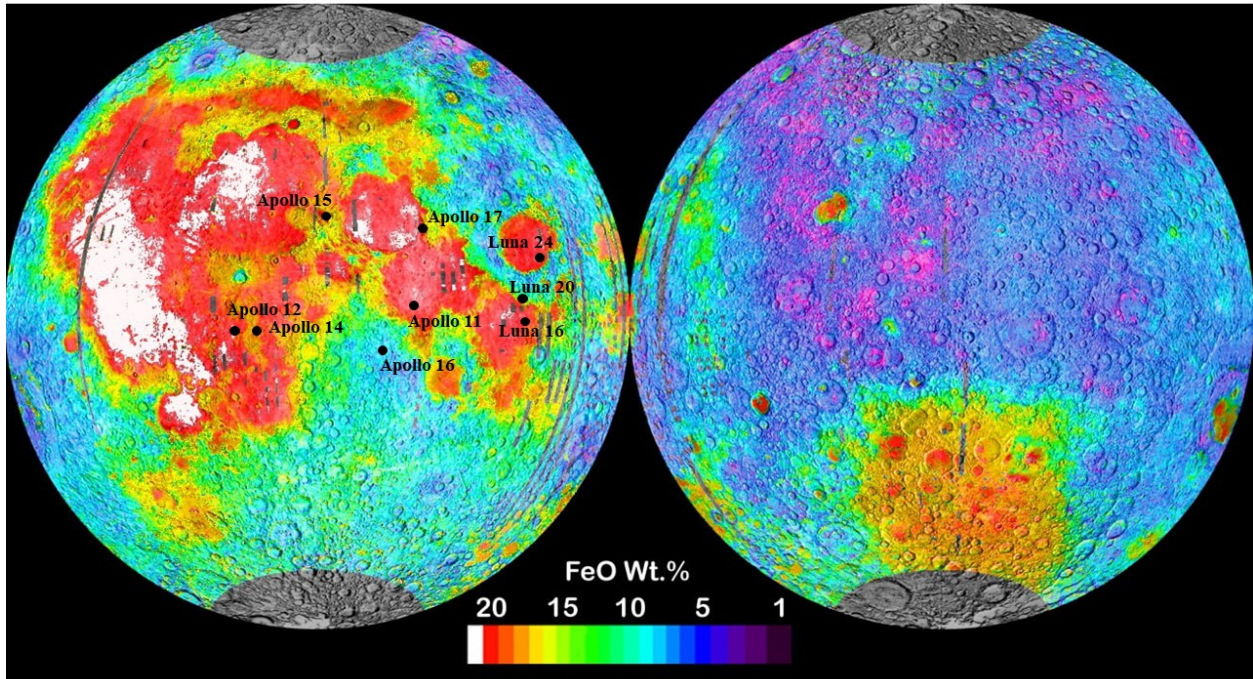
Fig. 1. Modified from https://sites.wustl.edu/meteoritesite/items/lunar-meteorites/ by R. Korotev.
FeO wt% map of the Moon with Apollo and Luna landing sites indicated.

Many source-crater paired meteorites are also basalt flow pairs, originating from the same basalt lava flow (Mijajlovic et al. 2020). Paired meteorites are linked together through similarities in composition, petrology, cosmic ray exposure, and crystallization ages. Furthermore, basaltic meteorites, such as those examined in this study, are even more rare, with only 30 distinct meteorites classified as basalts or basaltic breccias once fall pairings are considered. Therefore, lunar meteorites, and basaltic lunar meteorites especially, are an invaluable resource to the lunar sample inventory here on Earth.

Composition of Lunar Material

Lunar material comprises four major minerals: anorthite, olivine, pyroxene, and ilmenite. This relatively simple mineralogy is due to the restriction of major elements on the Moon. In decreasing order of abundance, O, Si, Al, Ca, Fe, Mg, and Ti are responsible for 99% of any given lunar sample's mass (Korotev 2005). Other minor and trace elements found in lunar rocks, include but are not limited, to SiO_2 polymorphs (i.e., cristobalite, tridymite, coesite), spinels [Fe, Mg Al and Cr oxides], tranquillityite [$(Fe^{2+}, Ca)_8(Zr,Y)_2Ti_3(SiO_4)_3O$; first discovered from the Apollo 11 basalts], kamacite [metallic FeNiCo], baddeleyite [ZrO_2], zircon [$ZrSiO_4$], troilite [FeS] (Korotev 2005), and phosphates/phosphides such as schreibersite [$(Fe, Ni)_3P$] (Pasek 2017). These minerals are found ubiquitously across the Moon, with differing concentrations of major and minor minerals depending on the lithology sampled. The Apollo and Luna mission samples are enriched in SiO_2 due to the free glass present in the regolith of the basaltic areas of the Moon sampled by these missions. Typically, the bulk concentration of SiO_2 is consistent at $43 - 46$ wt%, however lunar basalts have a much wider range of $38 - 48$ wt% (Korotev 2005). The significant differences between general lunar material (acquired from lunar meteorites) and the Apollo and Luna samples are a lack of Fe^{3+} unless present as a terrestrial weathering product, lack of sulfide apart from troilite, and an absence of carbonates and sulfates (Korotev 2005). Geochemical features of the distinct lunar lithologies are described below.

Lunar rocks occur in five distinct chemical compositions: anorthosites, magnesian suite non-mare rocks, high alkali suite non-mare rocks, KREEP rocks, and mare basalts. These lunar lithologies are not typical coherent rocks. Rather, the majority are polymict or monomict breccias, impact melt breccias, regolith breccias, granulitic breccias, fragmental breccias and unconsolidated lunar regolith. Anorthosites are composed of Ca-Al rich feldspars from the primary crust that formed the lunar surface (Joy and Arai 2013). This composition is distinct from the mare basalts, which contain lower quantities of Ca-Al rich feldspars due to a higher abundance in mafic minerals like pyroxene and olivine (Joy and Arai 2013). It is useful to distinguish between anorthosites and mare basalts using FeO and Al_2O_3 wt% as

basalts will be rich in iron and poor in aluminum (<15%) when compared with other highland/anorthosite rocks which are poor in iron but rich in aluminum (Korotev 2005). Basalts can further be divided into high-Ti basalts (1 – 6% TiO_2) or low-Ti basalts (6 – 14% TiO_2) with lunar meteorites typically containing 3 – 6% TiO_2 (Korotev 2005). Finally, lunar basalts have a negative Eu anomaly and feldspathic rocks a positive anomaly due to the substitution of divalent Eu for Ca^{2+} in plagioclase (Korotev 2005). KREEP rocks are distinct from other lithologies but can include rocks from the mare basalts, Mg-suite, and high alkali suite (Taylor 2009). The term KREEP stems from the incompatible-element enriched material produced by enrichment in potassium (K), rare earth elements (REE) and phosphorous (P). Six of the Apollo missions landed directly within the Procellarum KREEP terrane (PKT) with an additional three missions collecting samples near enough to the area to contain PKT ejecta from impact processes (Korotev 2005). This sampling resulted in a collection of lunar rocks that are mafic, Th-rich, impact melt breccias and glass, atypical of the lunar surface geology (See Fig. 2 for a summary of differing lunar compositions). While the Mg-suite and alkali suit are non-mare rocks, they differ from the feldspathic highland rocks due to their distinct chemical compositions resulting in troctolites and norites (Mg- suite), and quartz monzodiorites, felsites, and other alkali enriched lithologies (high-alkali suite) (Taylor 2009).

Impact Processes

Impact cratering is a ubiquitous geological process that affects all solid-surface planetary objects as it is governed by the same physics and fundamental processes regardless of its final target (Melosh 1989). It is through the natural process of hypervelocity collisions that meteorites are transported to other planetary bodies. Hypervelocity collisions are defined as an impact resulting from a cosmic projectile large enough to strike a planetary surface at cosmic velocities (>11 km/s, French 1998). The high pressures of these collisions at the point of impact (>100 GPa, Shoemaker 1960) produce shock waves that result in impact craters.

Impact craters are produced in three continuous stages: Contact and compression; Excavation; and Modification. These stages result in two general crater morphologies: simple craters and complex craters. Simple craters are bowl-shaped craters produced from impacts of relatively low shock pressures. The final crater rim of a simple crater will be approximately equal to the initial cavity rim formed during the collision. Complex craters contain steep walls that collapse under gravitational forces (Dence 1965), infilling an annular trough surrounding a central uplift.
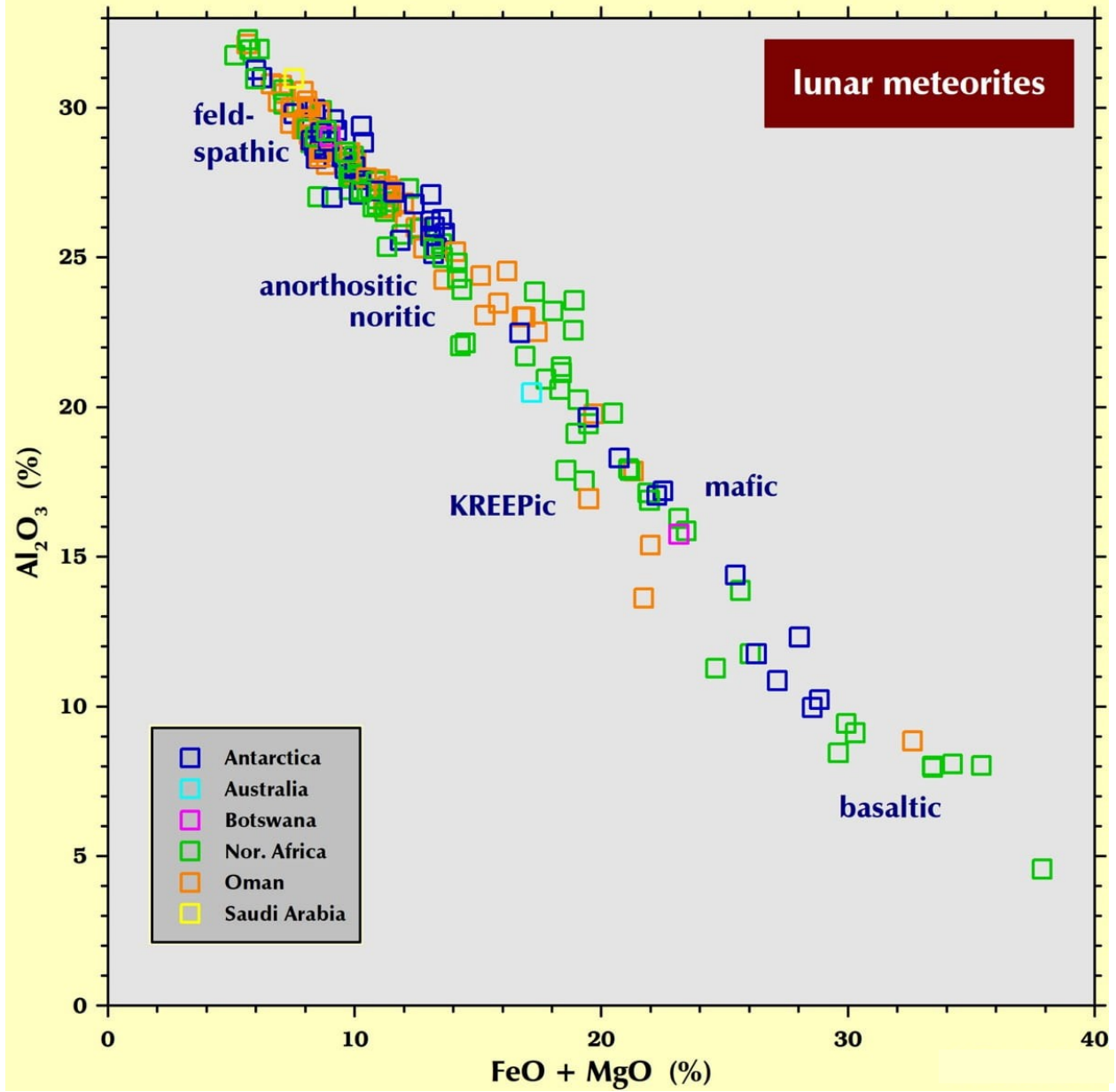
Fig. 2. Adapted from https://sites.wustl.edu/meteoritesite/items/lunar-meteorites-in-composition-space/ by R. Korotev, a chart of lunar meteorite composition based on FeO + MgO % vs Al_2O_3 %.

Ultimately, the gravitational instability of the material results in a downward and upward movement of target material producing the complex crater morphology (Osinski and Pierazzo 2013). During the first stage, the cosmic projectile makes contact with the target surface, penetrating to a depth of approximately 1 – 2 times its own diameter (O'Keefe and Ahrens 1982). This initial contact produces high-pressure shock compression waves which are then reflected back as a rarefaction wave (Melosh 1989) that reduces the density of the material due to the release of the compression. The rarefaction wave results in the vaporization of the projectile (Melosh 1989) which has no further bearing on the crater formation. The internal energy produced from the compression and rarefaction waves results in mineral deformation, transformation, and melting in both the target material within and surrounding the crater, as well as in the material ejected during the event that exceeds the escape velocity of the planetary body resulting in potential meteorites (Ahrens and O'Keefe 1972; Rubin 2015).

The first stage continues uninterrupted into the excavation stage in which the initial shock wave sets the target material into an outward radial motion (Osinski and Pierazzo 2013). While the shock wave sends material outwards, the rarefaction wave forces material downwards, which produces an excavation flow-field (Dence 1968) allowing for the exposure of subsurface geology. Once excavated, the forces eject the material ballistically beyond the cavity rim of the impact creating an ejecta blanket surrounding the crater (Oberbeck 1975). The velocity that ejected material must reach to escape the lunar surface and enter the Earth-Moon system is 2.78 km/s, however any faster will result in a heliocentric orbit that reduces the probability of the material landing on Earth and becoming a meteorite (Gladman et al. 1995).

The third and final stage of impact cratering is the modification stage. It is during the modification stage that the morphology of the final crater is dictated, due to both the target material lithology and the size of the cavity produced during the formation. Cavity diameter will dictate the formation of a simple or complex crater, while lithology dictates the pressures required to achieve the cavity diameters. Crystalline lithologies require larger impactor diameters to produce complex craters, while sedimentary targets require smaller impactor diameters to produce complex craters. On the lunar surface, the transition from a simple crater to a complex crater occurs between diameters of 15 and 27 km, whereas on Earth, complex craters form around cavities 4 km in diameter (Pike 1980). Despite being the final stage of crater formation, the modification of a crater has no marked end as geological processes native to the planetary surface such as mass movement and erosion tend to merge with the crater formation (Osinski and Pierazzo 2013). This makes the lunar surface a natural laboratory from

which to study crater formation and morphology as the low gravity, lack of atmosphere, and absence of aeolian, geologic, and aqueous processes allow for the prolonged preservation of craters that is not possible on Earth.

Hypervelocity collisions are also the process by which meteorites are delivered from the near-surface of their planetary bodies (Melosh 1985). A zone of interference between the shock and rarefaction waves and the zero-pressure free surface – called the spall zone – contains large, inverted pressure gradients that accelerate solid rock from depth to the velocities necessary to escape the gravity of their original bodies (Fig. 3). Due to the dynamics of hypervelocity collisions, all meteorites formed through ejection by the impact process will experience some form of shock metamorphism, also known as "shock". Shock effects in meteorites are observed on the microscopic scale in the form of mineral deformation, transformation, and melting. Over the last fifty years, significant experimental studies have been done regarding the effects of shock on quartz (e.g. French and Short 1968; Stöffler and Langenhorst 1994; Langenhorst 2002), feldspar (e.g. Bischoff and Stöffler 1992; Rubin 2015), olivine (e.g. Bischoff and Stöffler 1992; Schmitt 2000), and pyroxene (e.g. Rubin et al. 1997). These studies have allowed us to understand what shock deformation and transformation features occur within these minerals (e.g. planar deformation features, mosaicism, mechanical twinning, solid-state transformation) and what pressures are required to develop these features.

Shock is a complex process, highly influenced by heterogeneities in target properties such as composition, density, grain size, shape and orientation, presence or absence of volatiles, layering, pore space etc. Within a coherent rock, changes in density between minerals within an individual meteorite sample can produce shock effects suggesting a wide range of pressures. Sharp and DeCarli (2007) describe how frictional heating along shear bands forms shock melt veins while the collapse of open fractures and pores form shock melt pockets during shock wave compression. The experimental formation of shock melt veins (Kenkmann et al. 2000) has allowed us to relate the presence of the high-pressure minerals formed within them to source crater size estimates through comprehensive shock studies of meteorite samples. The majority of high-pressure minerals such as ringwoodite, bridgmanite and magnesiowüstite are found exclusively within and adjacent to the shock melt of a meteorite (Sharp and DeCarli 2007), while some SiO_2 polymorphs such as coesite and seifertite can be found within the bulk rock, always associated with silica glass (Miyahara et al. 2021).
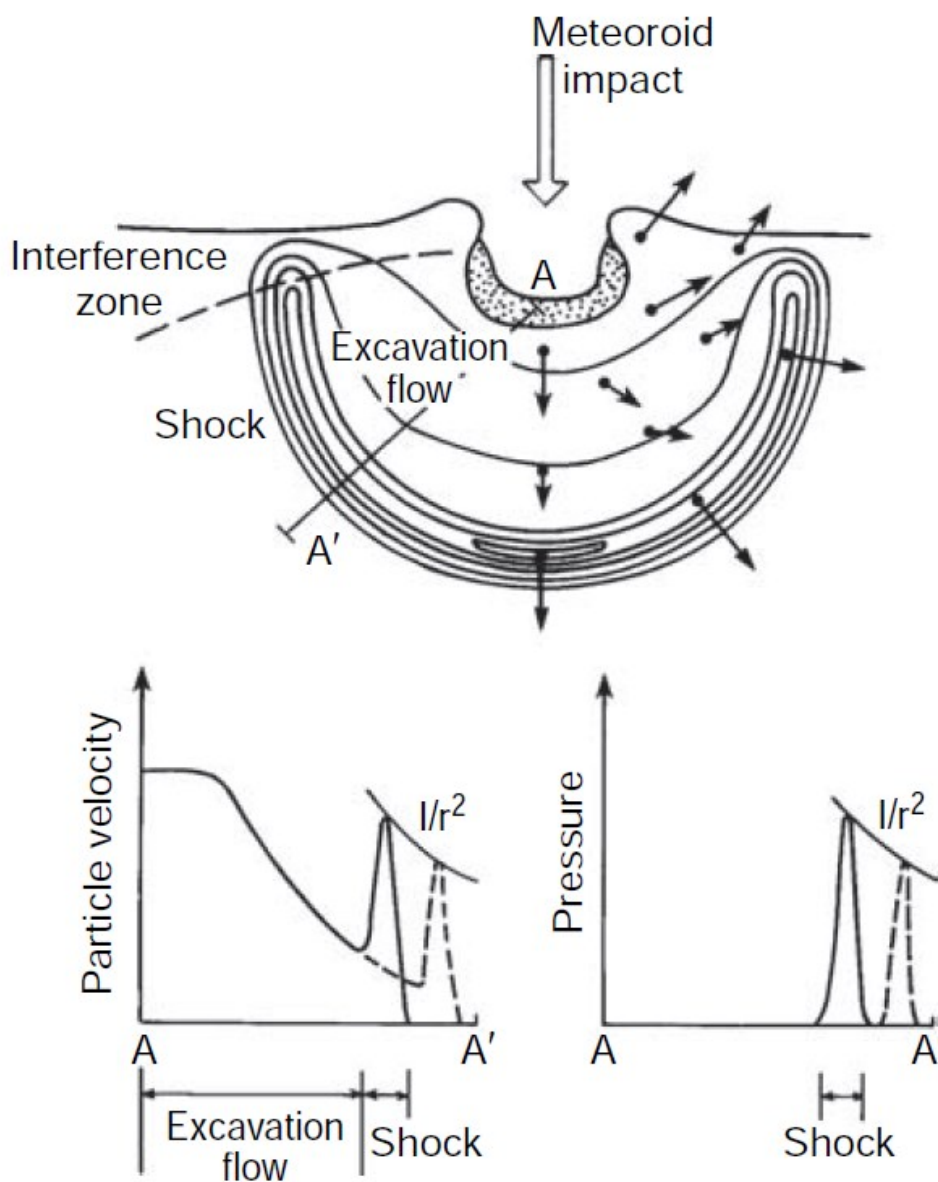
Fig. 3. Adapted from Melosh (2011). Illustrates the excavation flow following a meteorite impact. The graphs show the particle velocity and pressures across the cross-section AA' of the impact as a function of shock. The solid lines represent initial conditions with the dashed lines representing the conditions some time later.

The presence of high-pressure minerals within a meteorite can be the result of crystallization from the shock melt, or a solid-state transformation from a precursor host mineral. The pressure of the shockwave front is constant for a given volume of material at a specific distance from the point of impact, known as the bulk shock. The presence of high-pressure minerals within a meteorite can be the result of crystallization from the shock melt, or a solid-state pressure; however the recorded pressure in any given area of a sample, also known as the localized shock pressure, can vary by as much as an order of magnitude between mineral grains or within single grains (Sharp and DeCarli 2007).

Shock pressures and temperatures are independent of impactor size, instead being the product of a combination between the target lithology, impactor velocity, and location of the rock relative to the point of impact; therefore, shock metamorphic effects cannot directly indicate the crater size of the original launch site (Melosh 1989); high-pressure minerals observed during comprehensive shock investigations have been of use in estimating impactor size and crater diameter. Many studies, focused on Martian meteorites, have constrained the time a material has spent at high pressures, known as dwell time, to impactor diameter (Beck et al. 2005; Fritz and Greshake 2009; Walton et al. 2014; Bowling et al. 2020). One method to constrain the dwell time is to model the cooling rate of shock melt within the rock to determine the length of time the meteorite spent at peak pressure (Walton et al. 2014). The modelling done by Walton et al. (2014) is accomplished by acquiring a localized pressure-temperature constraint from the crystallization of new high-pressure minerals within the shock melt veins. The cooling rate of the shock melt is then estimated as a function of the apparent width of the melt vein where the high-pressure minerals are present. These minerals act as indicators for the shock pressure preserved at the time the melt crystallized. Depending on the location of the material ejected during the impact, the sample may occur within what is called the isobaric zone, or outside of it. Within the isobaric zone, the shock compression and release waves of the impact produce an equilibrium that allows for a nearly constant crystallization pressure for minerals within the shock melt (Asimow 2015; Fritz et al. 2017). During thermal quenching of the mineral assemblages within the shock melt, there is no significant decompression of the shock pressure due to the equilibrium within the isobaric zone. This equilibrium allows for the preservation of high-pressure minerals and the shock pressures they indicate (Sharp and DeCarli 2007). Samples that originate from outside this isobaric zone are shocked by an attenuated wave which, unlike the compression wave in the isobaric zone, undergoes immediate pressure decay. High post-shock temperatures within rocks located outside the isobaric zone allow the

minerals to back transform into lower-pressure phases due to the pressure decay experienced while the material is still cooling (Hu and Sharp 2022).

Study Overview

The goal of this thesis is to provide a comprehensive study of the shock metamorphism present in the unbrecciated basaltic lunar meteorites MIL 05035, NWA 10597, NWA 8632, NWA 4898, and NWA 479 to better constrain the shock conditions and impact histories of these samples and their paired stones. The bulk pressure – temperature conditions have been constrained by examining the shock effects within the meteorites such as mineral deformation (i.e., planar fractures, mosaicism) and transformation (i.e., shock-amorphized plagioclase hereby referred to as maskelynite), localized shock effects such as shock melt veins and pockets, and mineral crystallization from the shock melt. These features are then used to constrain localized pressure – temperature – time history which allow the estimation of shock duration and peak pressure. These conditions are then used, along with impact modelling, remote sensing, and geochemistry, to assist in determining the most likely source craters for the meteorites.

Chapter Two

Samples and Analytical Methods

A polished thin section of Northwest Africa (NWA) 10597 was made available for this study through loan from the Purple Mountain Observatory in Nanjing, China. A polished thin section of NWA 4898 was borrowed from Museum für Naturkunde in Berlin, Germany. The University of Washington in Seattle, WA provided a polished thin section and a tile of sample NWA 8632. NWA 479 is from the University of Alberta Meteorite Collection (specimen number MET11839). Finally, two thin sections (",31" and ",35") of Miller Range (MIL) 05035 were loaned through the US Antarctic Meteorite Program.

The composition of NWA 10597 is primarily zoned pigeonite (core: $En_{57.7-51.6}Wo_{8.9-16.8}$, rim: $En_{7.2-22}Wo_{20.2-31.5}$), augite ($Fs_{21.3-52.5}Wo_{28.4-39.3}$), zoned olivine (core: $Fo_{58.2-49.9}$, rim: $Fo_{36.6-40.7}$), plagioclase ($An_{78.5-87.8}Or_{0.2-0.8}$), and minor amounts of ilmenite, pyrrhotite, baddeleyite, apatite, merrillite, chromite, troilite, ulvöspinel, tranquillityite, zirconolite, and FeNi metal (Bouvier et al. 2017). NWA 4898 contains fewer minor phases with only FeNi metal, chromite, ilmenite, and troilite being present, while its major mineral composition is Ti-rich pyroxene ($Fs_{25.1-58.7}Wo_{13.2-34}$), olivine phenocrysts ($Fa_{26.3-27.2}$) and plagioclase ($An_{92.6-96.5}$) (Connolly et al. 2008). NWA 8632 is described as having both zoned olivine

phenocrysts (core: $Fa_{32.5-32.8}$, rim: $Fa_{48.8}$), and groundmass olivine ($Fa_{72.6-74.1}$) with a primarily elongated clinopyroxene groundmass ($Fs_{23.7-27.1}Wo_{40.1-40.5}$) and interstitial chromite and ilmenite (Ruzicka et al. 2014). No plagioclase was reported. NWA 479 is a paired stone of NWA 032 with olivine phenocrysts (core: Fo_{34-50}, rim: Fo_{30}) set in a groundmass of plumose plagioclase (An_{80-90}) intergrown with pyroxene ($En_{1-25}Wo_{15-25}$) (Grossman and Zipfel 2001). Lastly, MIL 05035 contains coarse grained pyroxene ($Fs_{31-55}Wo_{15-42}$) and plagioclase ($An_{83-92}Or_{0-2}$) with an intergrowth of fayalite-silica-and augite, and other minor amounts of sulfides, and iron-titanium oxides (Connolly et al. 2007).

Shock deformation effects such as mosaicism, undulose extinction, mechanical twinning, and planar fracturing were observed using an optical microscope, viewing samples in reflected, plane polarized, and cross polarized light. Samples were then further characterized using high resolution back scattered electron (BSE) imaging. BSE images were collected with a 20 kV accelerating voltage, using a ZEISS Sigma 300 field emission scanning electron microscope (FESEM) and Zeiss EVO LS15 scanning electron microscope (SEM) at the University of Alberta. The FESEM and EVO SEM are both equipped with a Bruker energy-dispersive X-ray (EDX) spectrometer used for mineral identification and glass composition by map and spot analysis acquisition. The FESEM EDX system has a dual silicon drift detector, measuring an area of 60 mm^2, and an energy resolution of 123 eV. The EVO SEM EDX system is equipped with a 10 mm^2 silicon drift detector with a 123 eV resolution.

The identification of high-pressure and amorphous phases of minerals were determined using a Horiba Scientific XPLORA-PLUS Raman spectrometer at MacEwan University, fitted with a four-grating turret. Samples were viewed using 5X, 10X, 20X, 50X and 100X objectives on a petrographic microscope integrated with the Raman system using reflected light. The Raman spectra were collected in confocal mode using a 785 nm laser, with the real volume resolution assessed to be <1.5 μm laterally and 2-3 μm in depth. The spectrum for each phase was collected in the Raman shift range of 100-1800 cm^{-1} using the 1800 gr/mm (grooves / millimeter) grating, to achieve a spectral resolution of 1.4 cm^{-1} at FWHM (full width at half maximum). The wavenumber accuracy was calibrated prior to daily use with the 520 cm^{-1} line of a silicon wafer. Small (micrometer-size) crystals in the vein matrix were located by viewing the thin section in reflected light and comparing the textures to those in BSE images. This Raman system was also used to assess the structural state of plagioclase and silica (crystalline versus amorphous), as the spectrum of glassy materials are characterized by broadened peaks in contrast to highly crystalline phases, which exhibit sharp peaks in the Raman spectrum (Fritz et al. 2005). The spectrum of pyroxene, olivine, silica, and plagioclase were acquired as seven 3-s exposures, which were then summed to

achieve the final spectrum. These minerals were analyzed using 50% of the full laser power (50 mW). Spectral backgrounds were graphically reduced using commercial spectroscopy software. Minerals were identified by their characteristic peak positions using a commercial searchable spectral library integrated with the Raman software, the online RRUFF Raman database and the published spectrum of individual minerals. Peaks in the spectrum were labelled using a Gauss Lorenz fitting.

The major and minor element composition of the plagioclase phase in NWA 8632 and silica in MIL 05035 was quantified using a JEOL 8900R electron microprobe analyzer (EPMA), equipped with five wavelength-dispersive spectrometers (WDS) at the University of Alberta. Twenty spot analyses were taken of the light grey silica phase, twenty of the dark grey silica phase, and eight of the plagioclase phase. Of the spot analyses, sixteen of the light grey silica phase, nineteen of the dark grey silica phase, and eight of the plagioclase phase provided data within acceptable totals. An accelerating voltage of 20 keV was used with a beam current of 20 nA for the silica grains and the same current with an accelerating voltage of 15 keV for the plagioclase, both with a focused beam. The following natural and synthetic materials were used for EPMA WDS analyses: diopside (Si, Ca), rutile (Ti), sanidine (Al, K), fayalite (Fe), forsterite (Fo), and albite (Na). Detection limits at the 99% confidence level for the analyzed elements were reported to be 0.020 (Si, Na), 0.026 (Ti), 0.015 (Al, Mg), 0.017 (Fe), and 0.009 (Ca, K) weight percent oxide.

Results

To quantify their compositions, individual EPMA WDS spot analyses were taken of the maskelynite grains in NWA 8632 and of the mottled silica texture in MIL 05035. The results of the analysis are summarized in Tables 1 and 2 below. High Fe and Ti in the maskelynite analyses were inferred to be from beam overlap with surrounding pyroxenes and Fe-Ti oxides, due to the small sizes (< 1 μm) of the maskelynite grains. Although EDS was used to find grains with the lowest possible Fe content, nevertheless Fe and Ti were too high for stoichiometric plagioclase. Table 3 displays recast data of the maskelynite EPMA analyses with Fe, Mg, and Ti removed.

Table 1. EPMA Analyses Light (A) and Dark (B) Grey Silica Mottling Texture in MIL 05035

A	1-LG	2-LG	3-LG	4-LG	5-LG	6-LG	7-LG	8-LG	9-LG
SiO_2	99.06	97.47	97.96	98.83	98.46	98.29	98.31	98.78	98.21
TiO_2	0.18	0.16	0.21	0.18	0.16	0.13	0.22	0.18	0.17
Al_2O_3	0.39	0.38	0.45	0.31	0.33	0.32	0.40	0.39	0.31
FeO	0.05	0.56	0.05	0.02	0.06	0.05	0.06	0.05	0.04
NiO	0.01	0.01	0.00	0.00	0.00	0.01	0.00	0.00	0.01
MnO	0.00	0.01	0.00	0.00	0.00	0.00	0.00	0.00	0.00
MgO	0.00	0.03	0.02	0.00	0.01	0.01	0.01	0.00	0.00
CaO	0.01	0.01	0.04	0.02	0.03	0.05	0.03	0.02	0.03
Na_2O	0.04	0.02	0.03	0.03	0.05	0.03	0.07	0.04	0.01
K2O	0.17	0.16	0.16	0.14	0.15	0.15	0.18	0.16	0.13
TOTAL	99.92	98.81	98.90	99.59	99.25	99.04	99.26	99.64	98.92
	10-LG	11-LG	12-LG	13-LG	14-LG	15-LG	16-LG	AVG	
SiO_2	98.30	98.64	98.38	95.73	98.61	99.03	97.87	98.25	
TiO_2	0.15	0.17	0.16	0.17	0.18	0.16	0.15	0.17	
Al_2O_3	0.35	0.36	0.37	0.35	0.34	0.32	0.34	0.36	
FeO	0.02	0.03	0.04	0.02	0.04	0.04	0.04	0.07	
NiO	0.00	0.01	0.00	0.00	0.00	0.00	0.00	0.00	
MnO	0.00	0.00	0.00	0.00	0.00	0.00	0.00	0.00	
MgO	0.01	0.00	0.01	0.00	0.01	0.01	0.00	0.01	
CaO	0.04	0.01	0.00	0.01	0.01	0.05	0.03	0.02	
Na_2O	0.04	0.04	0.02	0.03	0.04	0.01	0.02	0.03	
K2O	0.17	0.18	0.18	0.17	0.16	0.15	0.15	0.16	
TOTAL	99.09	99.46	99.17	96.49	99.44	99.77	98.61	99.07	

B	1-DG	2-DG	3-DG	4-DG	5-DG	6-DG	7-DG	8-DG	9-DG	10-DG
SiO_2	99.46	99.90	99.83	99.87	99.08	98.97	98.79	99.29	99.33	98.88
TiO_2	0.16	0.18	0.17	0.20	0.17	0.19	0.14	0.15	0.17	0.22
Al_2O_3	0.45	0.43	0.43	0.41	0.36	0.36	0.44	0.35	0.34	0.36
FeO	0.11	0.22	0.18	0.17	0.08	0.07	0.09	0.04	0.04	0.25
NiO	0.00	0.00	0.00	0.00	0.00	0.00	0.00	0.00	0.00	0.00
MnO	0.01	0.02	0.00	0.01	0.00	0.00	0.01	0.00	0.00	0.01
MgO	0.01	0.00	0.00	0.00	0.00	0.00	0.00	0.00	0.00	0.00
CaO	0.01	0.04	0.04	0.03	0.01	0.01	0.01	0.01	0.01	0.01
Na_2O	0.05	0.05	0.02	0.05	0.02	0.02	0.04	0.04	0.03	0.02
K2O	0.21	0.21	0.19	0.20	0.17	0.20	0.24	0.19	0.17	0.16
TOTAL	100.47	101.05	100.86	100.95	99.89	99.82	99.76	100.07	100.09	99.94
	11-DG	12-DG	13-DG	14-DG	15-DG	16-DG	17-DG	18-DG	19-DG	AVG
SiO_2	99.54	98.51	98.94	99.39	98.81	99.25	99.13	99.01	99.53	99.24
TiO_2	0.24	0.22	0.22	0.18	0.19	0.18	0.20	0.21	0.18	0.19
Al_2O_3	0.33	0.37	0.33	0.37	0.35	0.41	0.37	0.38	0.39	0.38
FeO	0.17	0.22	0.17	0.20	0.23	0.13	0.06	0.10	0.11	0.14
NiO	0.01	0.00	0.00	0.00	0.01	0.00	0.00	0.00	0.00	0.00
MnO	0.01	0.01	0.01	0.00	0.00	0.00	0.01	0.00	0.00	0.01
MgO	0.00	0.00	0.00	0.00	0.01	0.00	0.00	0.00	0.00	0.00
CaO	0.01	0.02	0.02	0.02	0.02	0.02	0.01	0.01	0.02	0.02
Na_2O	0.00	0.03	0.02	0.02	0.01	0.01	0.04	0.01	0.01	0.03
K2O	0.16	0.16	0.17	0.17	0.16	0.19	0.19	0.19	0.17	0.18
TOTAL	100.47	99.54	99.89	100.35	99.79	100.19	100.03	99.91	100.43	100.18

Table 2. EPMA Analyses of Plagioclase in NWA 8632 and Cation Ratios Based on 8 Oxygen

	1	2	3	4	5	6	7	8	AVG	
SiO_2	56.44	58.17	56.51	55.00	59.23	56.91	57.36	58.18	57.23	
TiO_2	0.55	0.79	0.35	0.67	0.38	0.47	0.53	0.44	0.52	
Al_2O_3	24.16	21.83	24.77	22.69	22.69	25.27	23.84	23.65	23.61	
Cr_2O_3	0.02	0.02	0.00	0.04	0.01	0.02	0.00	0.00	0.01	
FeO	3.96	5.01	3.22	6.04	2.92	2.93	2.92	3.78	3.85	
NiO	0.00	0.00	0.01	0.00	0.01	0.01	0.00	0.00	0.00	
MnO	0.04	0.08	0.02	0.07	0.01	0.02	0.02	0.04	0.04	
MgO	0.18	0.28	0.20	0.37	0.16	0.20	0.16	0.23	0.22	
CaO	12.88	12.38	13.54	13.10	12.71	13.57	13.02	12.99	13.02	
Na_2O	1.52	1.50	1.94	1.31	1.29	1.77	1.30	1.25	1.49	
K_2O	0.45	0.46	0.50	0.33	0.34	0.38	0.42	0.39	0.41	
P_2O_5	0.04	0.06	0.03	0.07	0.06	0.01	0.01	0.02	0.04	
TOTAL	100.24	100.58	101.09	99.69	99.81	101.56	99.58	100.97	100.44	
Cation Ratios	1	2	3	4	5	6	7	8	AVG	
Si	2.57	2.65	2.55	2.55	2.68	2.55	2.61	2.62	2.60	
Ti	0.02	0.03	0.01	0.02	0.01	0.02	0.02	0.01	0.02	
Al	1.30	1.17	1.32	1.24	1.21	1.33	1.28	1.25	1.26	
Cr	0.00	0.00	0.00	0.00	0.00	0.00	0.00	0.00	0.00	
Fe	0.15	0.19	0.12	0.23	0.11	0.11	0.11	0.14	0.15	
Ni	0.00	0.00	0.00	0.00	0.00	0.00	0.00	0.00	0.00	
Mn	0.00	0.00	0.00	0.00	0.00	0.00	0.00	0.00	0.00	
Mg	0.01	0.02	0.01	0.03	0.01	0.01	0.01	0.02	0.02	
Ca	0.63	0.60	0.66	0.65	0.62	0.65	0.63	0.63	0.63	
Na	0.13	0.13	0.17	0.12	0.11	0.15	0.11	0.11	0.13	
K	0.03	0.03	0.03	0.02	0.02	0.02	0.02	0.02	0.02	
P	0.00	0.00	0.00	0.00	0.00	0.00	0.00	0.00	0.00	
Total	4.84	4.82	4.87	4.87	4.77	4.85	4.80	4.80	4.83	
									max	min
Ab	0.17	0.17	0.20	0.15	0.15	0.19	0.15	0.14	0.19	0.14
Or	0.03	0.04	0.03	0.02	0.03	0.03	0.03	0.03	0.04	0.03
An	0.80	0.79	0.77	0.83	0.82	0.79	0.82	0.83	0.83	0.77

Table 3. Recast EPMA Analyses of Plagioclase in NWA 8632 and Cation Ratios Based on 8 Oxygen

	1	2	3	4	5	6	7	8	AVG	
SiO_2	59.07	61.56	58.07	59.39	61.47	58.10	59.77	60.28	59.71	
Al_2O_3	25.29	23.10	25.45	24.50	23.55	25.80	24.84	24.50	24.63	
Cr_2O_3	0.02	0.02	0.00	0.04	0.01	0.02	0.00	0.00	0.01	
NiO	0.00	0.00	0.01	0.00	0.01	0.01	0.00	0.00	0.00	
MnO	0.04	0.08	0.02	0.08	0.01	0.02	0.02	0.04	0.04	
CaO	13.48	13.10	13.91	14.15	13.19	13.85	13.57	13.46	13.59	
Na_2O	1.59	1.59	1.99	1.41	1.34	1.81	1.35	1.30	1.55	
K_2O	0.47	0.49	0.51	0.36	0.35	0.39	0.44	0.40	0.43	
P_2O_5	0.04	0.06	0.03	0.08	0.06	0.01	0.01	0.02	0.04	
TOTAL	100.00	100.00	100.00	100.00	100.00	100.00	100.00	100.00	100.00	

Cation Ratios	1	2	3	4	5	6	7	8	AVG	
Si	2.64	2.74	2.60	2.65	2.73	2.60	2.66	2.68	2.66	
Al	1.33	1.21	1.35	1.29	1.23	1.36	1.30	1.28	1.29	
Cr	0.00	0.00	0.00	0.00	0.00	0.00	0.00	0.00	0.00	
Ni	0.00	0.00	0.00	0.00	0.00	0.00	0.00	0.00	0.00	
Mn	0.00	0.00	0.00	0.00	0.00	0.00	0.00	0.00	0.00	
Ca	0.64	0.62	0.67	0.68	0.63	0.66	0.65	0.64	0.65	
Na	0.14	0.14	0.17	0.12	0.12	0.16	0.12	0.11	0.13	
K	0.03	0.03	0.03	0.02	0.02	0.02	0.02	0.02	0.02	
P	0.00	0.00	0.00	0.00	0.00	0.00	0.00	0.00	0.00	
Total	4.78	4.74	4.82	4.77	4.72	4.81	4.76	4.74	4.77	
									max	min
Ab	0.17	0.17	0.20	0.15	0.15	0.19	0.15	0.14	0.2	0.14
Or	0.03	0.04	0.03	0.02	0.03	0.03	0.03	0.03	0.04	0.02
An	0.80	0.79	0.77	0.83	0.82	0.79	0.82	0.83	0.83	0.77

Shock Deformation and Transformation in Host-Rock Minerals

MIL 05035 contains coarse-grained pyroxene and plagioclase (grain size up to 1.5 mm). Olivine (grain size ~10 μm) is present in a symplectite - a vermicular intergrowth of fayalite, augite, and silica. The pyroxene and olivine minerals display extinction patterns that vary between individual grains. Pyroxene grains display two types of extinction: wave-like alternating patterns of extinction characteristic of undulose extinction (Fig. 4b); and mosaicism, as indicated by some pyroxene crystals that show domains of mottled extinction (Fig. 4c). Mosaicism is also present in the olivine crystals (Fig. 4a). Thin open fractures occur in two distinct orientations intersecting at 90˚ within olivine crystals, spaced 1 – 2 μm apart (Fig. 4d). These planar fractures are observed in only a portion of the olivine crystals present in the meteorite and when they occur within the individual grains, they are restricted to only a portion of the grain.

The amorphous plagioclase is almost entirely isotropic in cross-polarized light upon stage rotation, with small, 20 μm size birefringent islands within an otherwise isotropic grain (Fig. 5b). In BSE images, the plagioclase feldspar is homogenous, with few fractures (Fig. 6b). No apparent zoning, indicated by a change in grey scale that varies from core to rim, is observed. The grains lack vesicles or flow structures characteristic of melting. Spot mode Raman spectra taken of the isotropic areas of the feldspar grains display broadened peaks centered around 500 cm^{-1} and 1000 cm^{-1} (Fig. 6c). Raman spectra taken of the birefringent islands were noisy, with a small peak at 468 cm^{-1}, an intense peak at 516 cm^{-1} and a small peak at 1002 cm^{-1} (Fig. 5c).

NWA 10597 is composed of pyroxene, olivine, plagioclase, and silica. Medium grained pyroxene crystals (100 μm) show a change in grey scale from core to rim in BSE imaging. Olivine phenocrysts measure up to 200 μm in length with coarse-grained tabular plagioclase exceeding lengths of 600 μm. Silica grains measure up to 200 μm. Coarse grains of ilmenite can also be observed, measuring as large as 200 μm. Silica appears as a smooth dark phase in BSE imaging, with some areas containing a mottled light-dark pattern within the grain (Fig. 7b). Raman spectroscopy of the dark grey areas revealed broadened peaks centered around 480 cm^{-1} and 600 cm^{-1} (Fig. 7c). The lighter grey areas showed a range light-dark pattern within the grain (Fig. 7b). Raman spectroscopy of the dark grey areas revealed broadened peaks of spectral characteristics with four distinct spectra emerging: two broad peaks at 200 and 409 cm^{-1} with a broad valley between the two, a similar spectrum with more minor peaks and a slightly higher shift at 201 and 413 cm^{-1} and a small peak at 317 cm^{-1} in the broad valley, and finally a series of distinct peaks at 160, 282, 406, and 472 cm^{-1} with a sharp, intense peak at 516 cm^{-1} (Fig. 8).
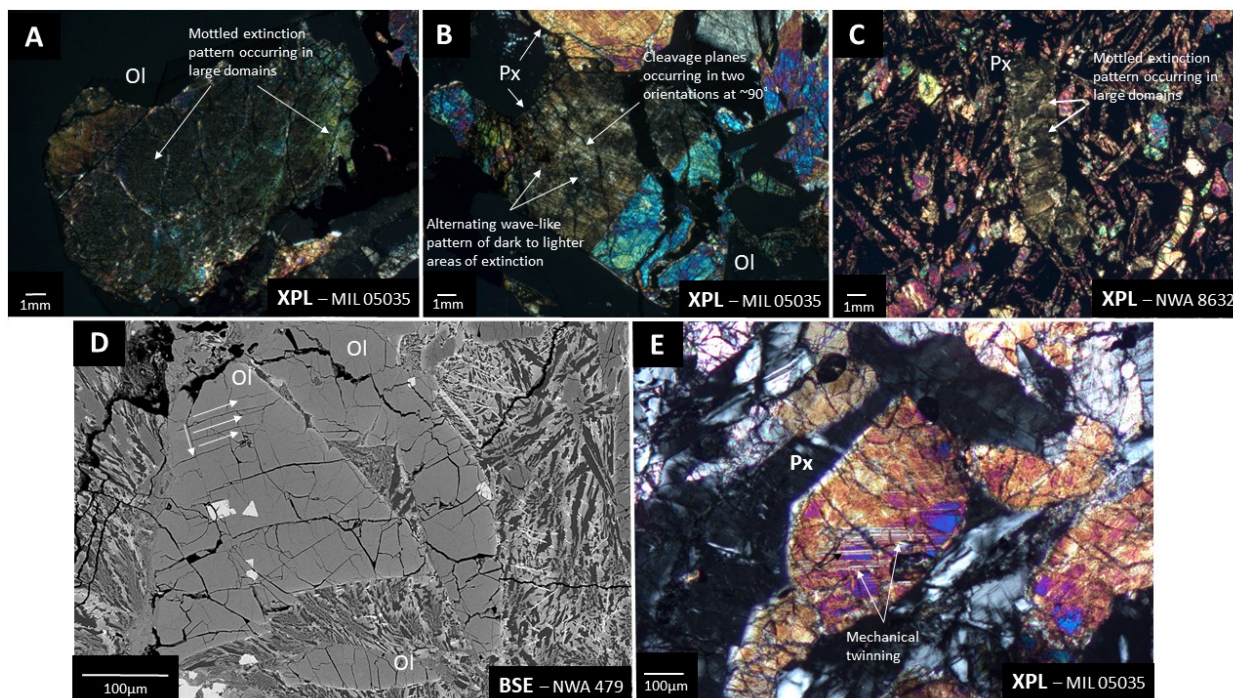
Fig. 4. Representation of shock deformation within host rock minerals present throughout the samples of this study. A) Mottled extinction of high interference colours in cross-polarized light indicates mosaicism of olivine. B) A wave-like extinction pattern of alternating dark and lighter areas characteristic of undulose extinction. The lower interference colours and ~90 ˚ intersection of cleavage planes identify this mineral as pyroxene. C) Pyroxene also shows the same mottled extinction pattern as olivine mosaicism in a few of the samples. D) Planar fractures in olivine occur as thin, open fissures within the mineral in two distinct orientations. The fractures have a heterogenous distribution both within a single mineral and throughout a sample. E) Mechanical twinning of pyroxene is also present in a few select samples such as NWA 10597 and MIL 05035. Mechanical twinning appears in cross-polarized light as thin, white, parallel fissures. Mechanical twinning is not observed in back-scattered electron imaging distinguishing it from planar fractures and cleavage plane.
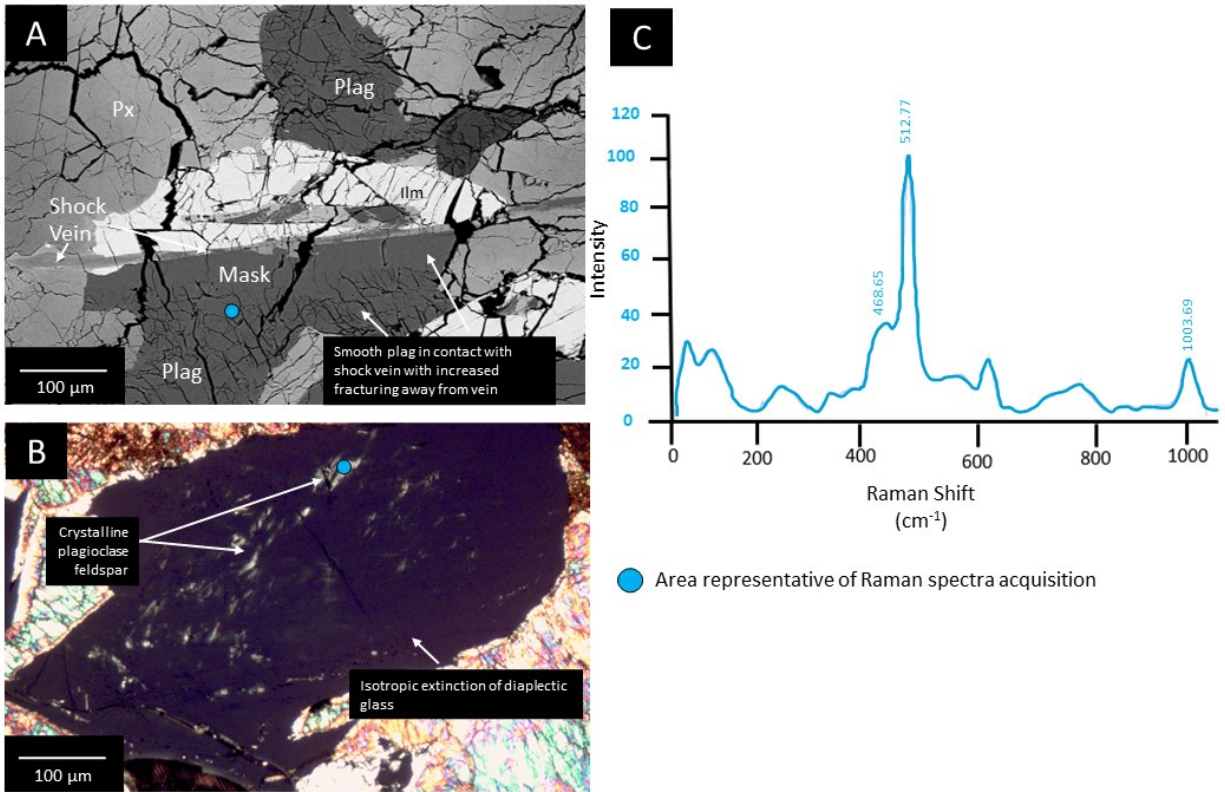
Fig. 5. A) Grains of plagioclase composition in NWA 10597 display partial maskelynization evident in BSE imaging. Grains at some distance from the shock melt are highly irregularly fractured, becoming less so closer to the melt until the plagioclase closest to the shock melt becomes smooth and homogenous, with no presence of flow textures or vesicles to suggest melting. B) Optical image taken in XPL from sample MIL 05035 showing a mostly isotropic maskelynite grain with small crystalline plagioclase feldspar fragments still present. C) Raman spectra from these areas show a distinct peak at 520 cm^{-1} confirming a crystalline anorthite phase.
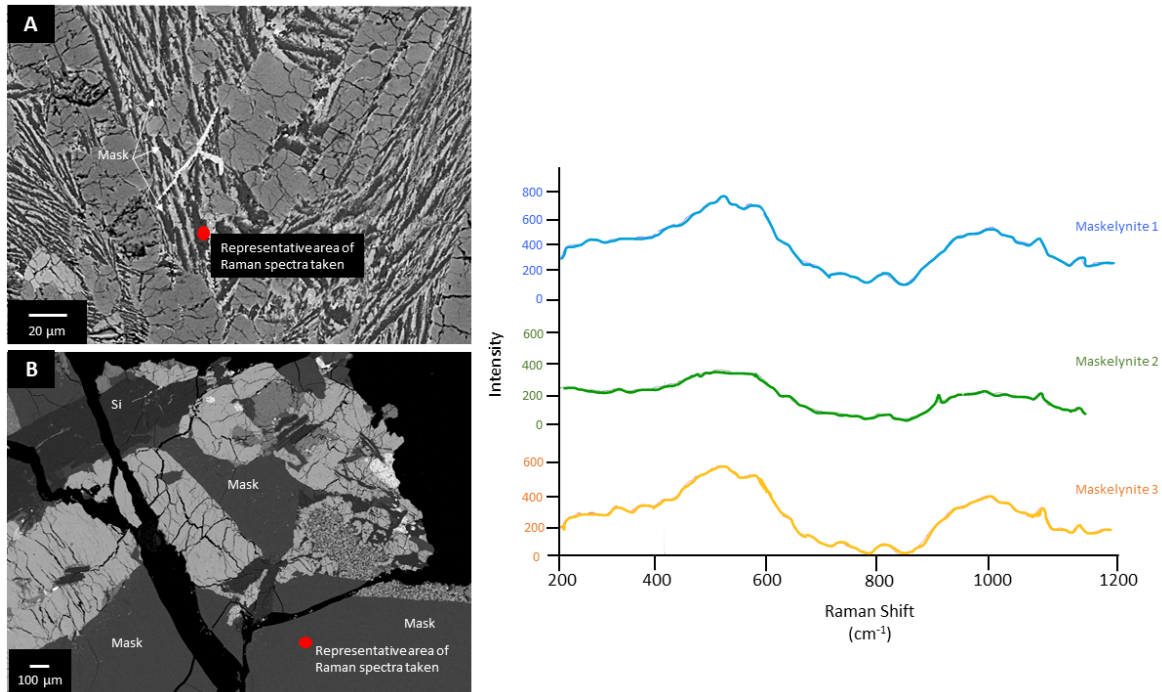
Fig. 6. A) Grains of plagioclase composition in samples NWA 8632, NWA 10597, NWA 4898 and NWA 479 are fine-grained (< 10μm) groundmass crystals intergrown with pyroxene. In BSE imaging, the plagioclase grains are smooth and homogenous, with no vesicles or flow textures present. Example from [meteorite name here] B) Plagioclase grains in MIL 05035 are coarse-grained measuring ~ 1.5mm in width. Similar to the aforementioned samples, in BSE imaging the grains are smooth and homogenous, with no evidence of vesicles or flow textures. When Raman spectra of these grains were taken, they consistently showed broad peaks centered around 500 cm^{-1} and 1000 cm^{-1} (right). The spectra lack the well-defined peaks of crystalline plagioclase feldspar suggesting an amorphous material. This, coupled with BSE imaging, suggest a solid-state transformation of the plagioclase feldspar to diaplectic glass (maskelynite).
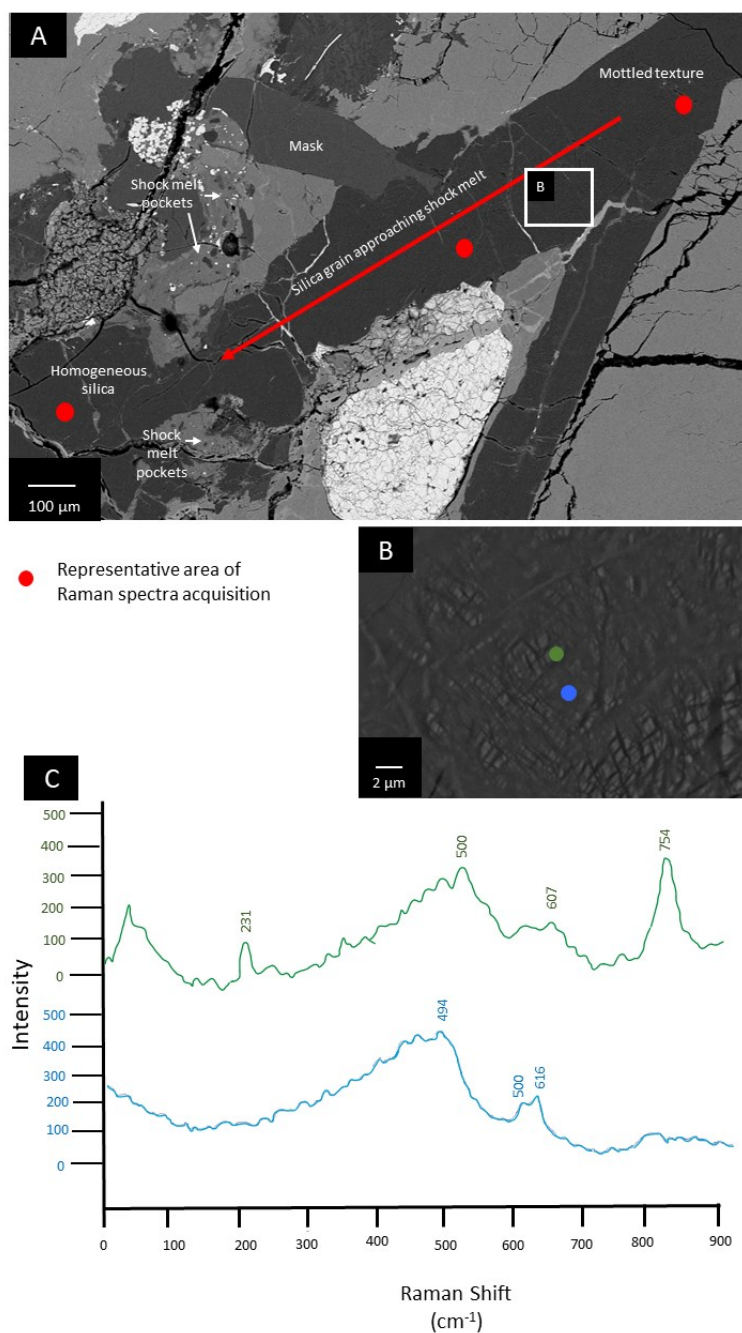
Fig. 7. The silica phase in MIL 05035 A) cross cuts fractured maskelynite. As the silica approaches the shock melt, the texture becomes increasingly homogenous, as the intensity of the mottled texture in B) decreases. C) Raman was taken of the dark grey and light grey silica phases in two different areas. The dark grey phase produced an amorphous spectrum characterized by a broad hump around 494 cm^{-1} and the light grey phase produced a stishovite spectrum identified by the distinct peak at 754 cm^{-1}.

22
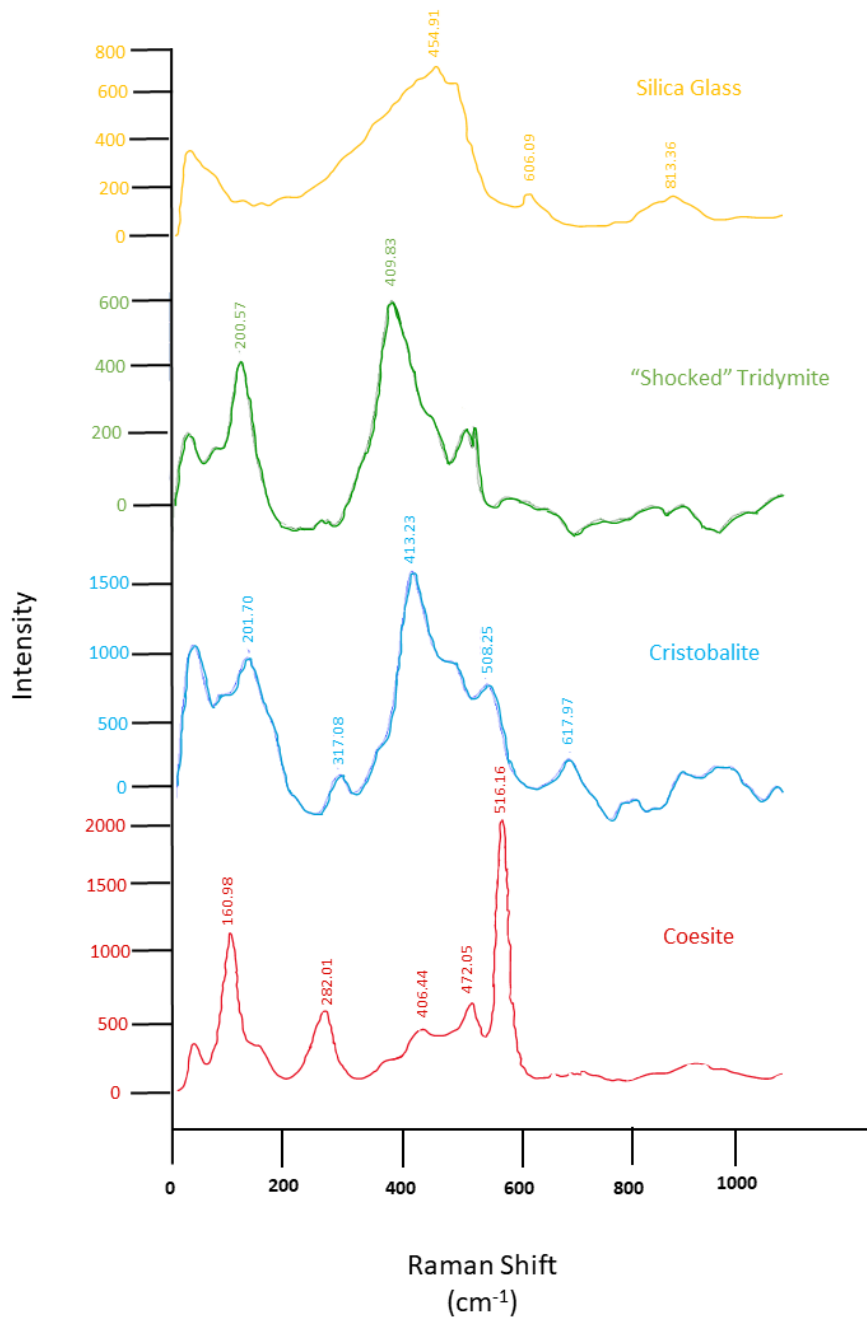
Fig. 8. Raman spectra of the different structures of silica observed in NWA 10597. NWA 10597 contained not only amorphous glass displaying broad peaks around 454 and 606 cm^{-1}, but other crystalline structures such as strongly shocked tridymite displaying a wide valley separating two distinct peaks at ~ 200 and 410 cm^{-1}, cristobalite, which contains more peaks than the tridymite including a slightly higher shifted peak at 415 cm^{-1}, and coesite, which is characterized by a distinct peak around 520 cm^{-1}.

Under BSE imaging the plagioclase grains show two distinct textures within single grains depending on the distance to shock melt. Large amounts of irregular fracturing were observed in grains and parts of the grains distant from shock veins and shock melt pockets. With proximity to shock melt, the plagioclase becomes smooth and homogenous with vesicles or flow structures present (Fig. 5a). Raman spectra of the homogenous areas show broad bands centered around 500 cm^{-1} and 1000 cm^{-1} (Fig. 6c). When viewed in cross polarized light, the plagioclase grains display white to light grey interference colours (maximum birefringence δ = 0.013). These small islands of birefringent areas are observed within an otherwise isotropic grain (Fig. 6b). The Raman spectra of these islands produced distinct peaks at 469 cm^{-1} and 516 cm^{-1} and other smaller peaks at 656 cm^{-1}, 818 cm^{-1}, and 1003 cm^{-1} (Fig. 5c).

When viewed in cross-polarized light, olivine phenocrysts exhibit weak mosaicism and undulose extinction is observed in pyroxene (Fig. 4a,b). Planar fractures were observed in olivine in two distinct orientations measuring 2 – 3 μm in width and spaced 20 – 30 μm apart (Fig. 4d). Mechanical twinning was observed in pyroxene, appearing as thin, parallel fissures, in one orientation heterogeneous throughout the mineral, and visible in cross-polarized light (Fig. 4e).

NWA 4898 is characterized by a groundmass of elongated, tapered intergrowths of plagioclase and pyroxene measuring up to 30 μm and 40 μm, respectively. Single large crystals (300 μm) of olivine are also present in this meteorite. When viewed under cross-polarized light, olivine and pyroxene display weak mosaicism upon stage rotation (Fig. 4a,c). The grains of plagioclase feldspar were best viewed in BSE imaging, which shows a homogenous grey scale indicating a lack of zoning. The smooth grains lacked the irregular fractures found in olivine and pyroxene. Indications of melting, such as vesicles, and schlieren flow textures were not present (Fig. 6a). Raman spectra taken of these smooth plagioclase grains revealed the same broadened spectrum centered around 500 cm^{-1} and 1000 cm^{-1} (Fig. 6c).

Both NWA 8632 and NWA 479 are paired with the lunar meteorite NWA 032 (Korotev and Irving 2021) and as such all have similar textures. These meteorites have a fine-grained groundmass composed of elongated pyroxene crystals ~40 μm in width, arranged in a plumose texture with fine grained (<2 μm) plagioclase feldspar. The plagioclase was difficult to observe directly via transmitted light due to the fine grain size. In contrast, the coarse grain size of olivine phenocrysts (>400 μm) made observations of shock deformation effects in this mineral straightforward. The olivine in both meteorites contain open

fissures approximately 2 µm in wide, spaced 20 – 100 µm, occurring in two distinct orientations. These planar fractures are heterogeneously distributed throughout the samples and within the individual olivine grains in which they were observed (Fig. 4d). Both NWA 479 and NWA 8632 display undulose extinction in pyroxene (Fig. 4b). Additionally, mottled extinction patterns with large domains characteristic of weak mosaicism in both pyroxene and olivine crystals were observed when under cross-polarized light (Fig. 4a). In BSE imaging, plagioclase feldspar grains are a homogenous dark grey and arranged in the same plumose texture as the pyroxene (Fig. 6a). At most, the grains measured 10 µm in width. There were no fractures observed within the grains; instead, they had a smooth appearance lacking any vesicles or schlieren flow features. Further analysis of the plagioclase feldspar using Raman spectroscopy showed broadened bands centered around 500 cm^{-1} and 1000 cm^{-1}(Fig. 6c).

All meteorite samples were observed in transmitted polarized light. The maximum birefringence of olivine and pyroxene was found to be δ=0.050 and δ=0.021, respectively with no discolouration of the crystals observed.

Localized Shock Effects: Shock Veins and Shock Melt Pockets

When viewed in plane polarized light, anastomosing networks of shock veins and shock melt pockets from MIL 05035, NWA 10597, NWA 479 and NWA 8632 appear as honey-to sepia-coloured glass cutting across the igneous host rock (Fig. 9a,b). When viewed in cross polarized light, the shock melt is isotropic, with only the entrained minerals visible (Fig. 9c). Shock melt in NWA 4898 was not initially visible via transmitted light and had to be observed using BSE imaging due to shock melt veins and pockets measuring no larger than 20 µm in width. BSE imaging of thin section MIL 05035,35 revealed shock veins that cut across igneous host rock minerals with thinner shock veins connected to pockets of shock melt. The apparent width of the shock veins ranges from 10 – 40 µm while the shock melt pockets are significantly larger, up to 300 µm in length (Fig. 10a,b). Internal textures of the shock veins are predominantly glassy, while the shock melt pockets contain schlieren-rich flow structures observed as streaky grey scale variations in BSE images (Fig. 10a). Spheres of Fe-sulfides measuring 2 – 5 µm, identified by EDX spot analysis, were observed embedded in silicate glass (Fig. 10c). Shock melt contacts with plagioclase are diffuse, as are the boundaries between the melt and entrained Ca-phosphates. Micrometer sized crystals were also found nucleating along the walls of the host rock-shock melt contacts, as well as from the margins of rounded mineral clasts entrained in the shock melt (Fig. 10c).
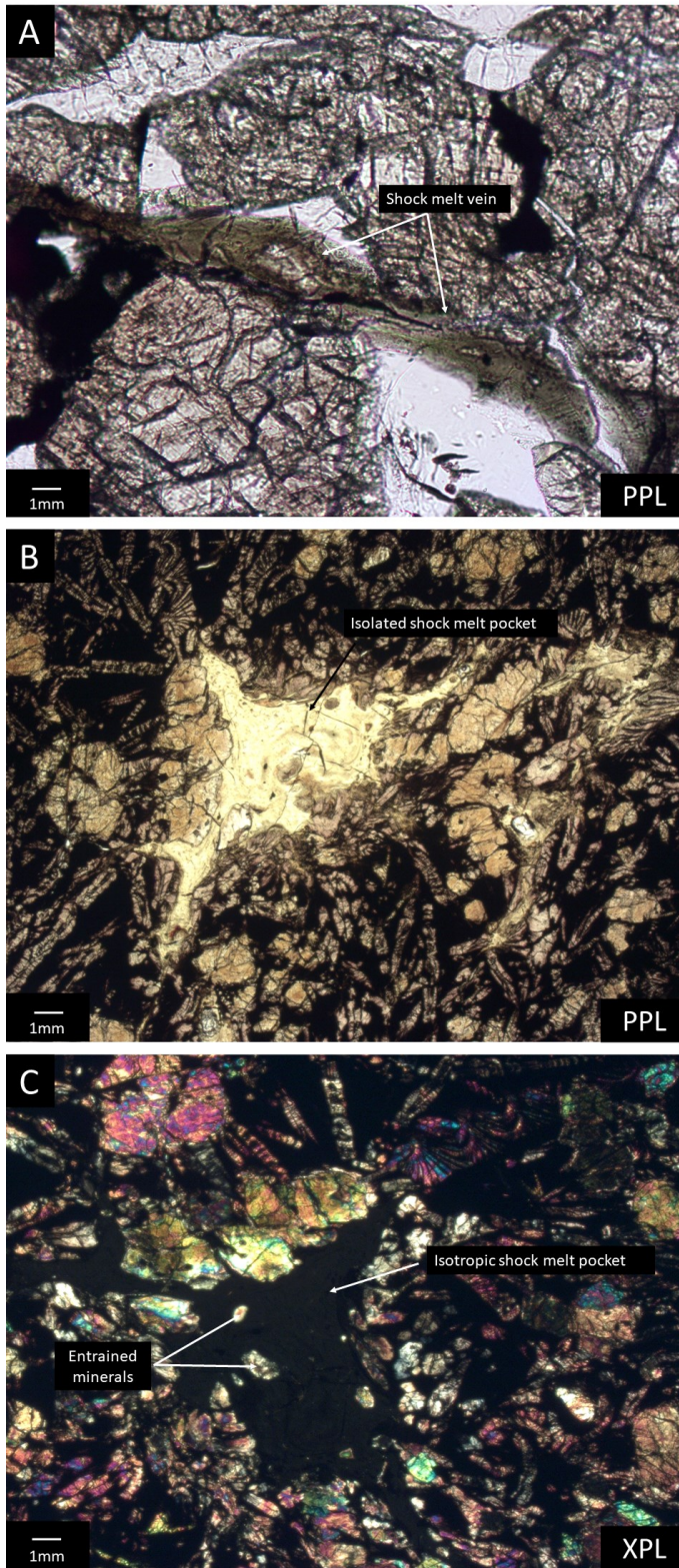
Fig. 9. A) A sepia-colour shock vein in plane polarized light representative of the transmitted light appearance of the shock melt in all the thin section samples. B) A honey-colour shock melt pocket in plane polarized light representative of the transmitted light appearance of shock melt in the thin section samples. Entrained minerals can be seen within the melt pocket and become more apparent in C) the cross polarized light view of the same melt pocket showing the resulting glass as extinct (isotropic).
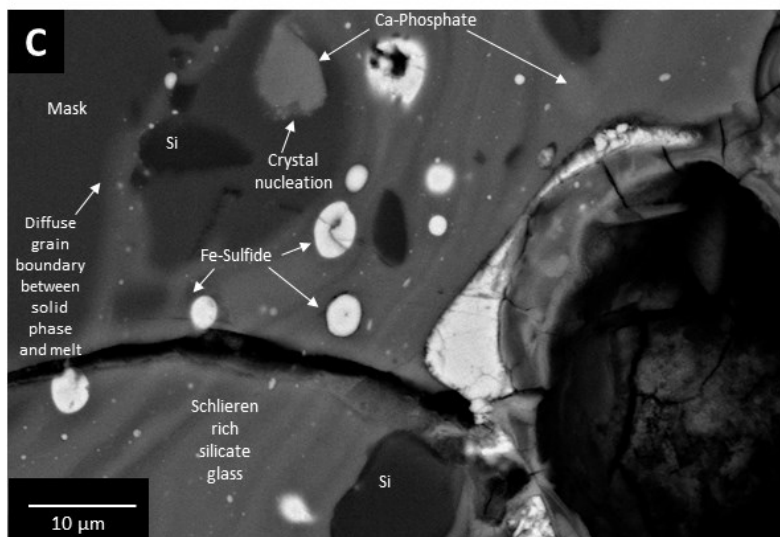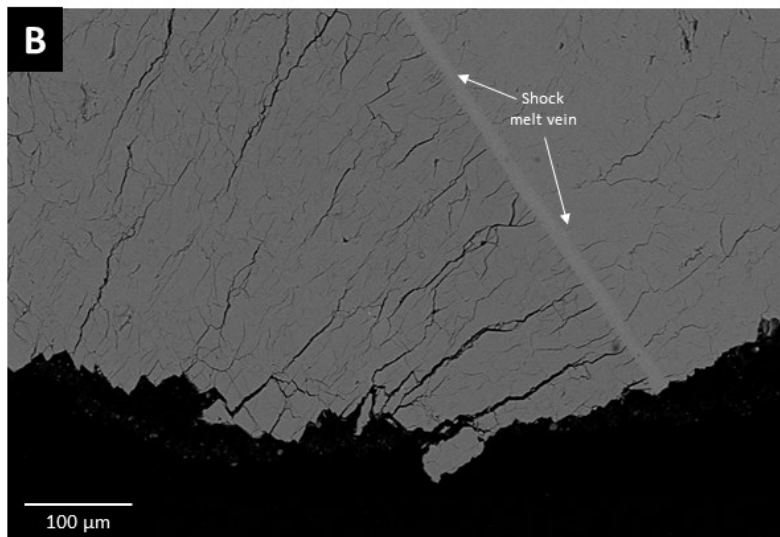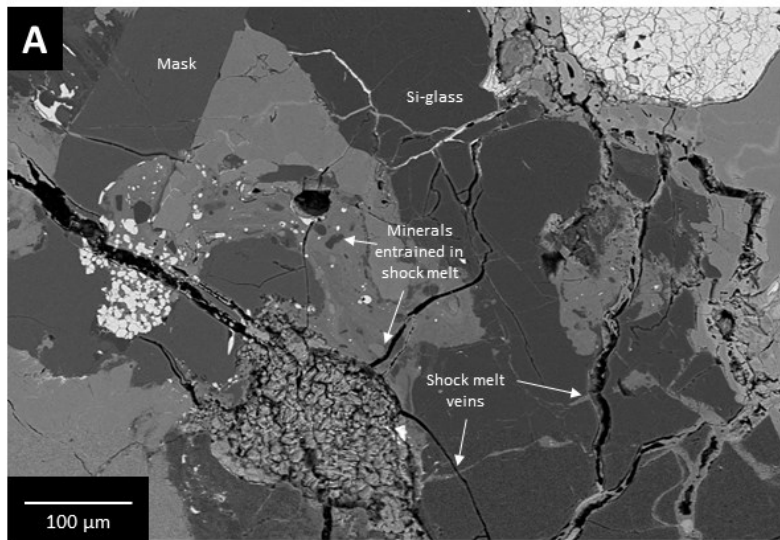
Fig. 10. Overview of shock in MIL 05035 in BSE. A) An extensive shock melt network of veins and pockets with minerals entrained in the melt and shock veins that B) cut across the igneous host rock. C) Crystal nucleation occurs from the margins of minerals entrained in the shock melt. Diffuse grain boundaries between the plagioclase and the melt are visible. Bright spheres of Fe-sulfides form immiscibility textures within the schlieren flow textures of the melt.

A range of grey scales was observed not only between minerals but within individual grains (core to rim) suggesting multiple phases and compositional zoning. Major element composition from EDX spot analysis revealed these minerals to be Mg-Fe-rich silicates. Raman data spot analysis of these minerals produced two distinct spectra. The first spectrum was ambient pressure pyroxene with a triplet at 319 cm^{-1}, 353 cm^{-1}, and 390 cm^{-1}, with sharp, well-defined peaks at 662 cm^{-1} and 837 cm^{-1}(Fig. 11). The second spectrum was that of ambient pressure olivine with a doublet at 809 cm^{-1} and 837 cm^{-1} (Fig. 11). MIL 05035 contains large tabular silica crystals (>1 mm). These crystals cross-cut large grains of maskelynite, distinguishable in BSE by their different grey scales, with silica being significantly darker than the maskelynite. Large, open fractures radiate from the silica grain boundary into neighboring mineralogy including cutting across maskelynite grains (Fig. 7a).

The majority of silica grains appear smooth and uniform dark grey in BSE images; however, a subset of silica grains exhibits a lighter mottled texture (Fig. 7b). This texture is observed within the large tabular grains (~1 mm length), as well as within the smaller 5 μm size silica grains found within the symplectite. One of the large silica grains is in contact with a shock melt pocket. In this grain the intensity of the mottled texture decreases as the grain approaches the shock melt (Fig. 7a). EDX spot analysis showed silica with minor amounts of aluminum present in both phases, with 1.4 wt% and 0.4 wt% Al_2O_3 content in the dark and light phase, respectively. Raman spectroscopy of the two phases revealed an amorphous silica spectrum for the dark grey phase with a significant peak at 605 cm^{-1}. The light grey phase was finer grained, measuring up to 2 μm in length. This fine grain size meant that the spectrum has a mixed signature with contributions to the Raman signal from the surrounding silica. The spectrum shows a broad peak at 500 cm^{-1}, a small peak at 607 cm^{-1}, and a sharp, distinct peak at 754 cm^{-1} indicative of stishovite (Fig. 7c). Raman spot analysis of the symplectite silica was attempted, however no usable spectrum was achieved as the spectra either completely lacked signal or showed small signals from the surrounding crystalline minerals (olivine, pyroxene).

The BSE imaging of the NWA 479 tile revealed an abundance of schlieren rich shock veins measuring 4 – 40 μm in width. These veins cut through the groundmass and the phenocrysts of the host rock, forming an anastomosing network. Large pockets of melt up to 500 μm in width were observed within in the network, as well as isolated from it (Fig. 12b). Mineral clasts are entrained in the shock melt of both the veins and the pockets, with new crystal growth nucleating around them, as well as on the melt margins (Fig. 12a). New crystal growth ranged in size from <1 μm to a maximum of 2 μm. Raman spectra of these crystals was consistent with that of olivine and pyroxene (Fig. 11).
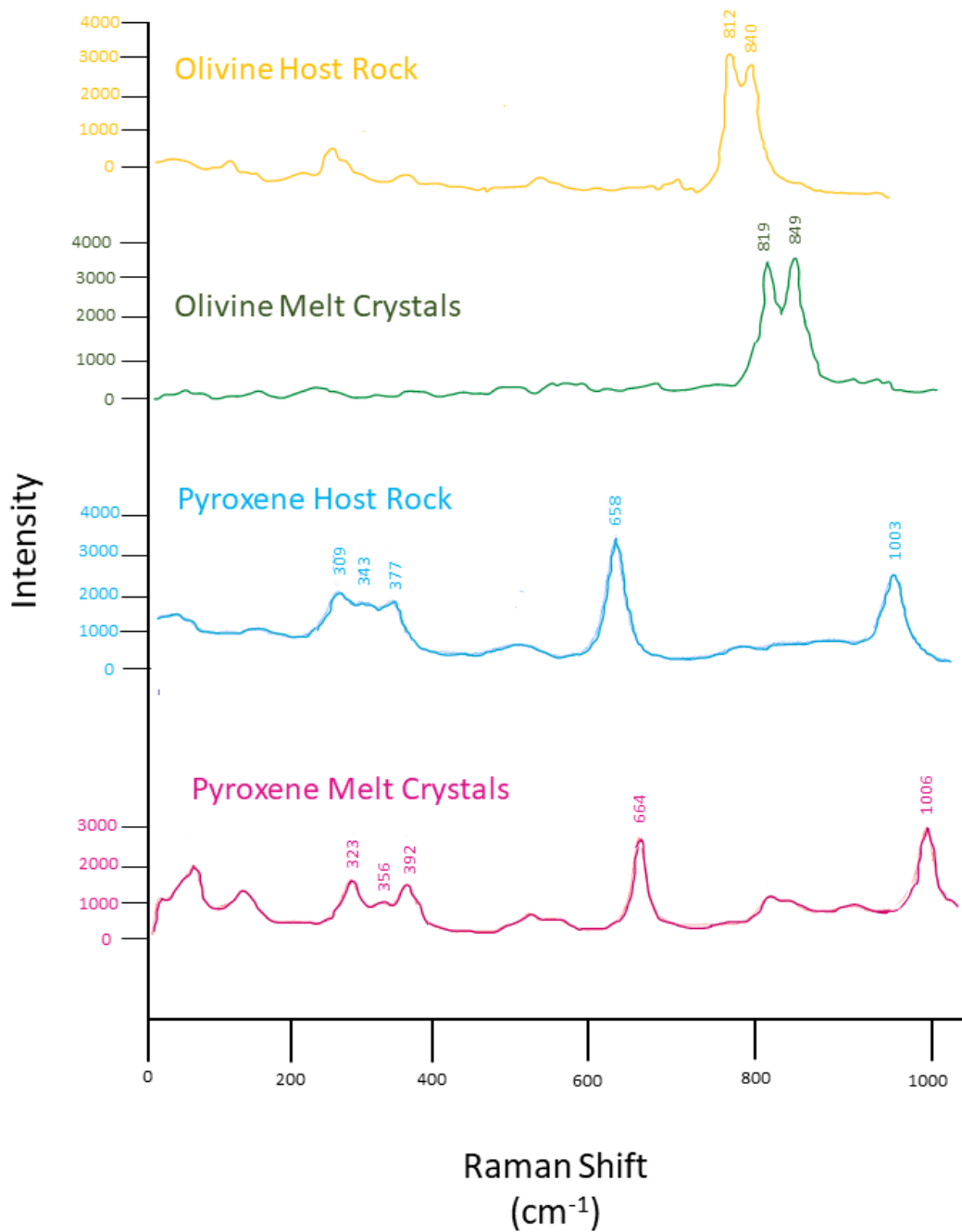
Fig. 11. Representative Raman spectra comparing host rock minerals to that of the crystals nucleating within the melt of the meteorite samples. Both the olivine and pyroxene spectra display sharp, distinct peaks indicative of crystalline material with peak positions of low-pressure phases for both the host rock minerals and melt crystals.
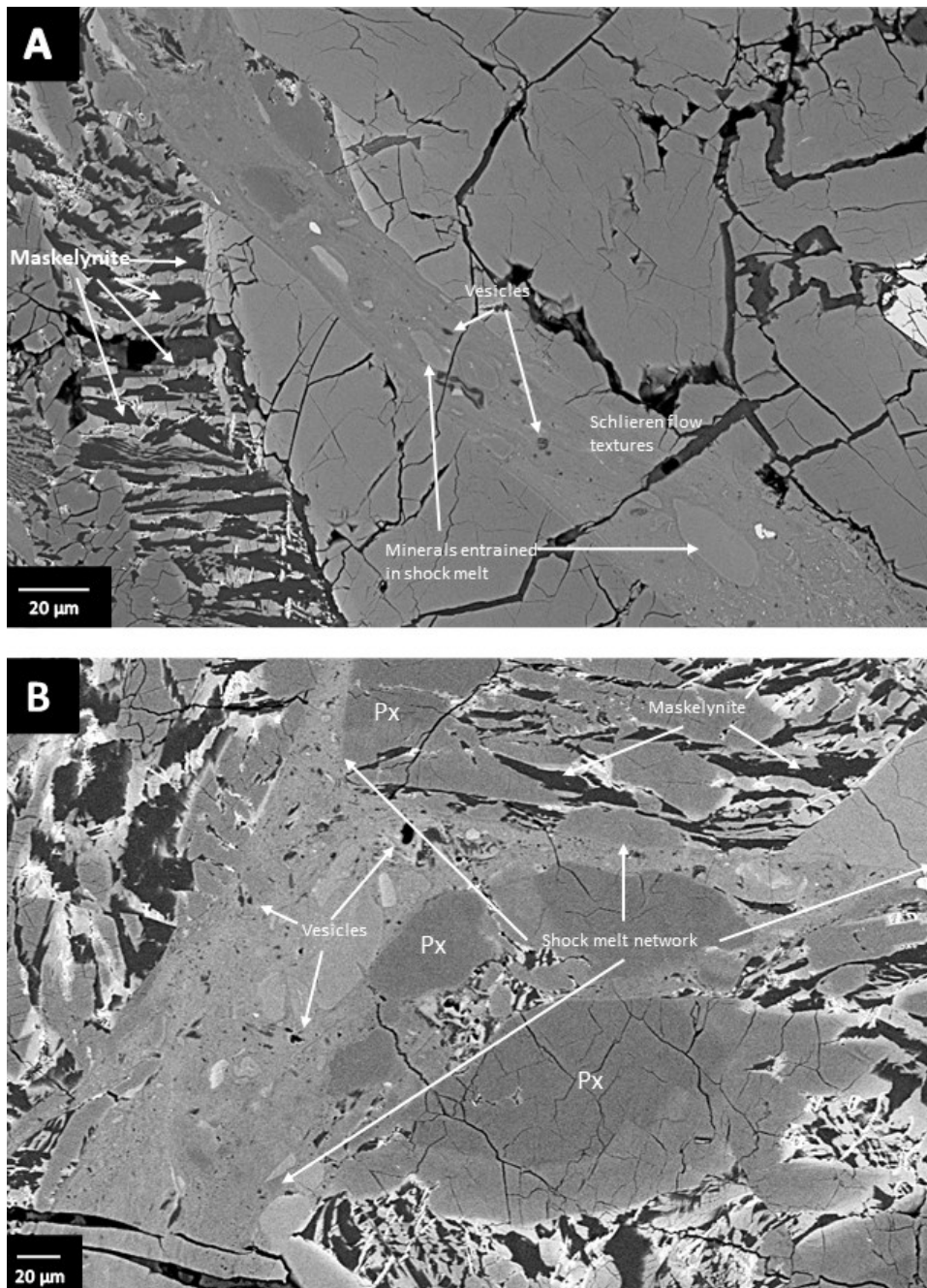
Fig. 12. NWA 479 has A) shock veins cutting across host rock igneous minerals and fine grained maskelynite in the areas surrounding the melt. Minerals of varying sizes can be seen entrained in the melt. B) Shock melt in the sample forms complex networks of pockets and veins throughout. The melt is distinguishable in BSE imaging by the flow textures, immiscibility textures, and numerous vesicles present within it.

The olivine spectra display a doublet at 813 and 843 cm^{-1} while the pyroxene spectrum presents a triplet at 323 cm^{-1}, 356 cm^{-1}, and 392 cm^{-1} with peaks at 664 cm^{-1} and 1006 cm^{-1}, specifically indicating an augite composition. One of the minerals entrained in the shock melt presents a characteristic olivine doublet; however, the peaks measured were shifted to a lower wavenumber at 789 cm^{-1} and 841 cm^{-1} (Fig. 13a,b). This peak position (789 cm^{-1}) is characteristic of ringwoodite, a high-pressure polymorph of olivine. Within the spectra is a distinct peak at 691.20 cm^{-1}, interpreted as Raman signal contribution from surrounding pyroxene crystals.

Like the previously described samples, NWA 10597 displays a network of shock veins and shock melt pockets that cut through the igneous host rock (Fig. 14a). The veins measure 5 – 50 µm in width and the shock melt pockets have diameters as large as 100 µm. Similar to MIL 05035, spherical Fe-sulfides are present in schlieren-rich shock melt that appear as bright, micrometer sized spheres in BSE imaging (Fig. 14b). Fragments of host rock olivine and pyroxene are entrained within the shock melt and appear to have acted as sites of heterogenous nucleation for micrometer sized crystals. These same crystals were found nucleating from the margins of the shock melt. The thinnest shock veins (~5 µm wide) are almost completely crystallized (Fig. 14c). Raman analysis of these crystals nucleating from the shock melt show that they are olivine and pyroxene (Fig. 11). Some of the crystals, associated with the darker grey of silica grains, showed an increasing intensity of peaks at 406 cm^{-1}, 472 cm^{-1}, and 515 cm^{-1}, indicative of coesite (Fig. 8).

NWA 4898 contains thin shock veins measuring 2 µm – 40 µm wide cutting across the igneous host rock. Small pockets of shock melt were also observed, no larger than 20 µm in diameter, with diffuse boundaries where the melt is in contact with the surrounding maskelynite (Fig. 15a). Both the melt pockets and veins are rich in schlieren flow features and contain vesicles throughout. Micrometer sized crystals were found nucleating within the center of shock melt pockets as opposed to the margins of the shock melt as observed in previous samples (Fig. 15b). Raman spectra was collected of these micrometer minerals as well as the entrained host rock minerals, with both crystal spectrum types being characteristic of low-pressure olivine and pyroxene (Fig. 11).

BSE images of NWA 8632 reveal a complex network of shock veins that measure 10 – 100 µm in width with interconnected pockets of shock melt measuring up to 500 µm in diameter (Fig. 16a). Both the shock melt veins and pockets are predominantly glassy with schlieren flow textures and vesicles (Fig. 16b).
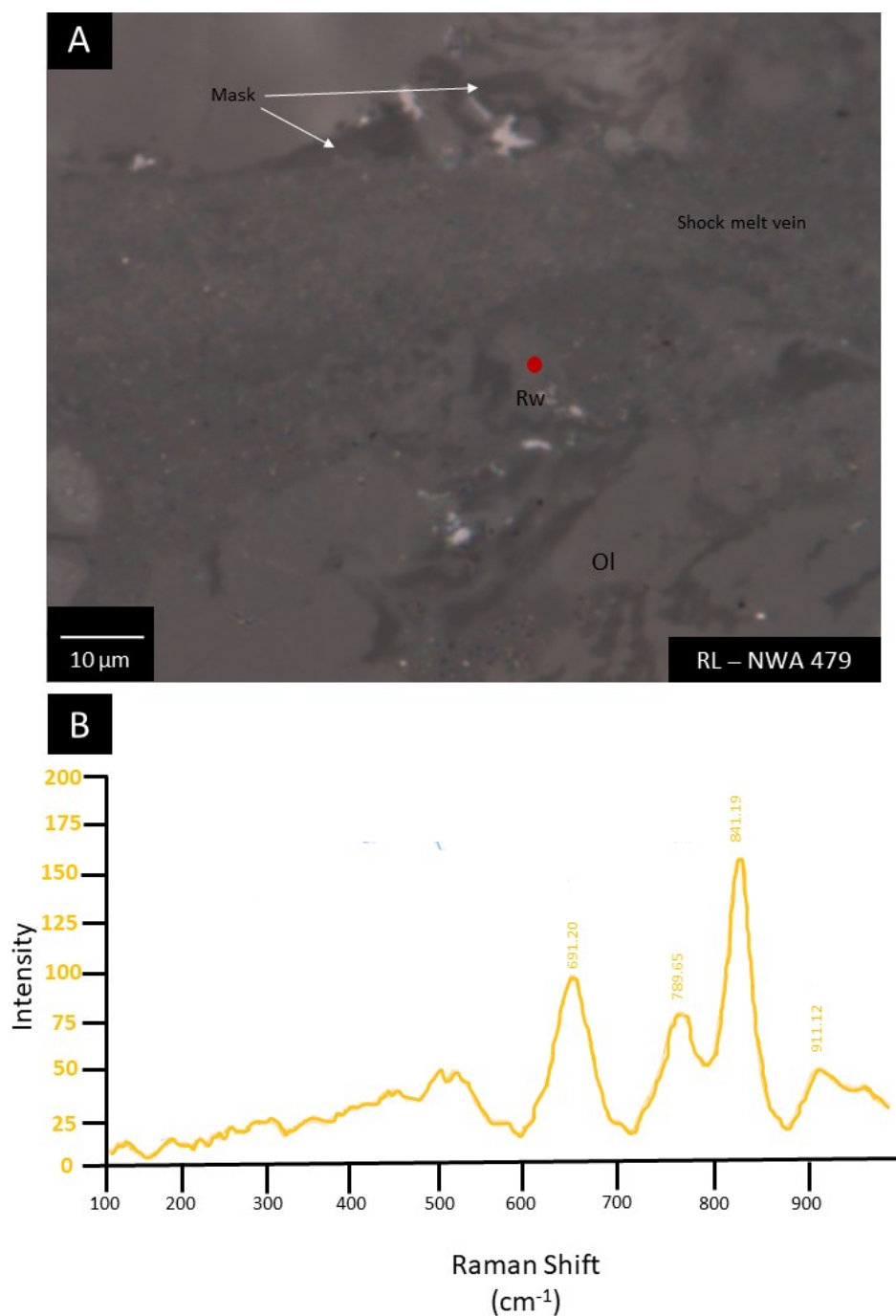
Fig. 13. A) Reflected light image taken of the ringwoodite crystal analyzed using Raman spectroscopy (red dot). The mineral is seen surrounded by shock melt that contains micrometer sized minerals inferred to have crystallized from the melt. The Raman spectrum associated with the spot analysis is also displayed (B), showing a doublet peak at 799 cm^{-1} and 844 cm^{-1} which is consistent with the spectrum of ringwoodite.
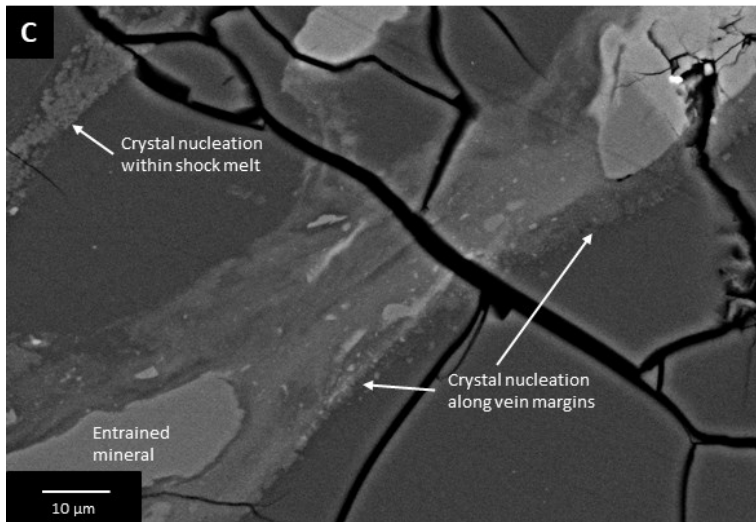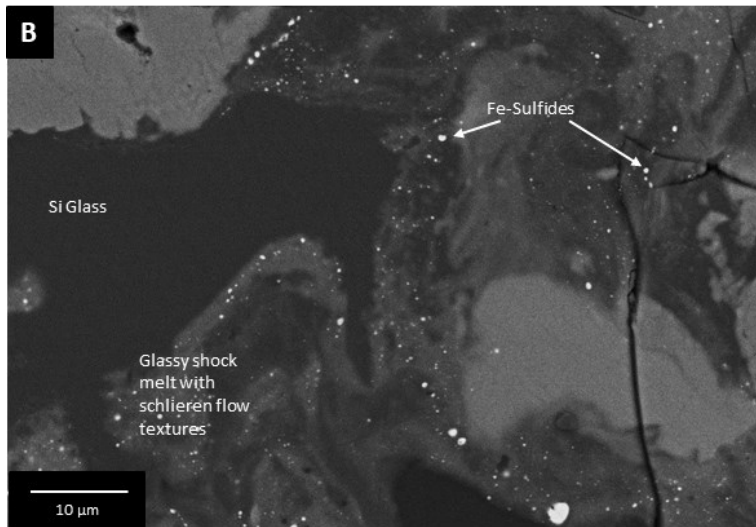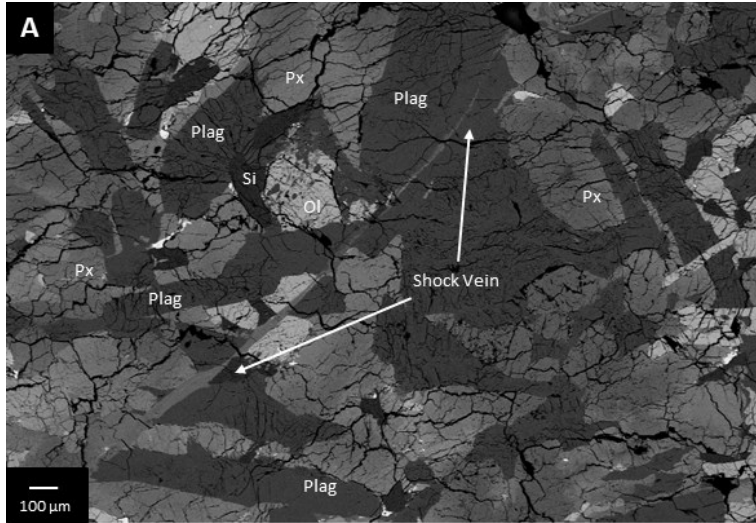
Fig. 14. A) Thin shock veins can be seen cutting across numerous igneous minerals within the host rock of NWA 10597. B) The melt pocket is glassy with small spheres of Fe-sulfides present in the melt due to their immiscibility. Schlieren flow textures can also be seen with pockets characterized by a streaky grey-scale. C) Minerals are entrained within the melt providing heterogeneous nucleation sites, with micrometer sized crystals also nucleating within the melt and from the shock melt margins.
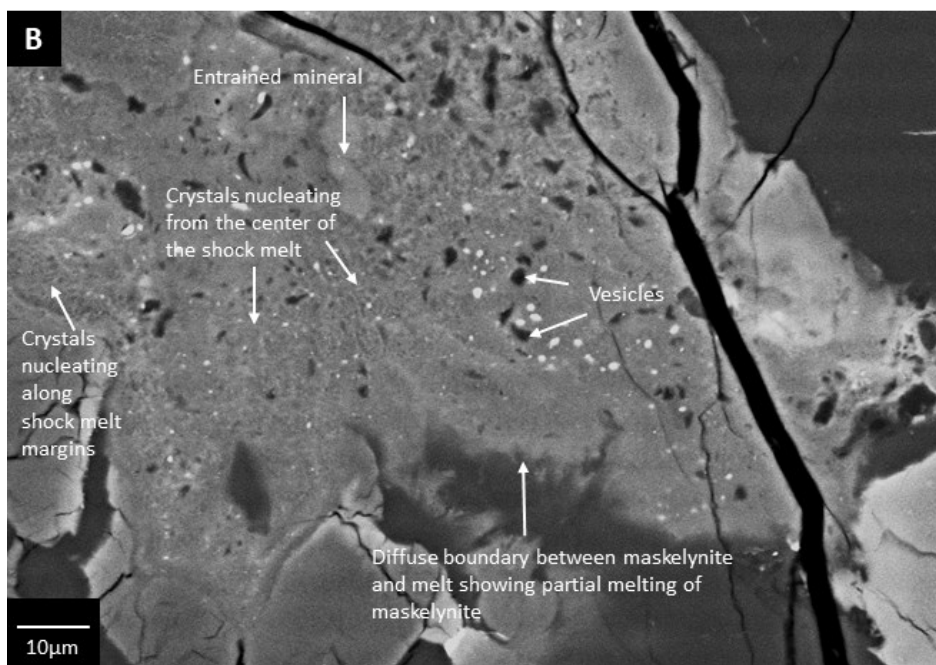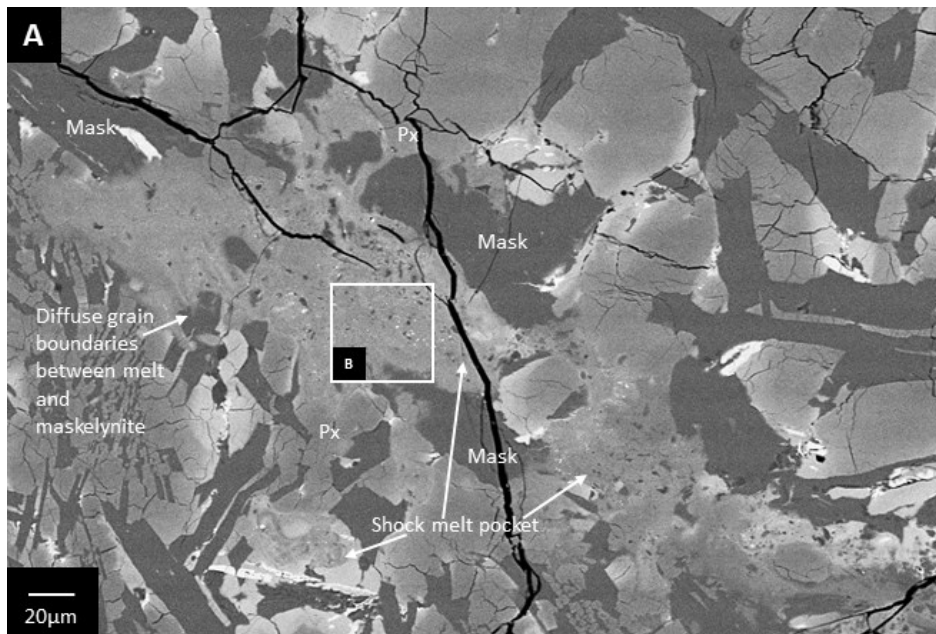
Fig. 15. A) NWA 4898 contains isolated melt pockets as well as melt pockets connected by a network of shock veins. The pockets contain bright Fe-sulfide spheres, vesicles, and flow textures. B) A close-up view of the melt pocket reveals micrometer sized crystals nucleating from the center of the melt as well as along the margins of the melt pocket. A dark grey, homogenous grain is interpreted to be maskelynite partially melting into the pocket as the boundary between the two is diffuse.
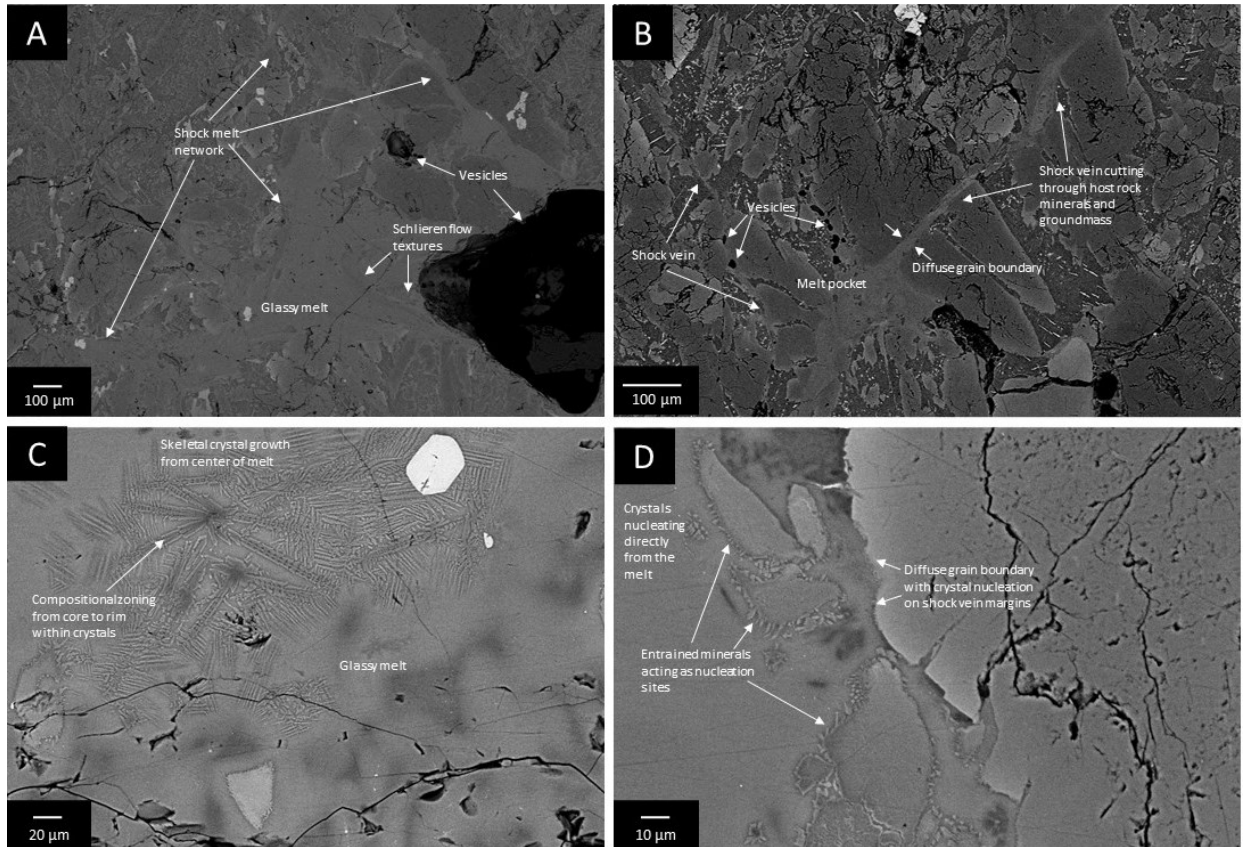
Fig. 16. Shock melt in NWA 8632 is connected through A) a network of melt pockets and veins ranging in size up to 100 μm. Vesicles can be seen associated with the shock melt along with schlieren flow textures and glassy areas. B) Melt can be seen cutting through igneous host rock minerals with diffuse boundaries occurring between the melt and the surrounding mineral grains C) within the apparent glassy melt, acicular crystals, measuring no more than 1μm in width can be seen crystallizing. The grey scale of the BSE imaging changes from core to rim indicating compositional zoning. D) Minerals entrained in the shock melt act as sites of heterogeneous nucleation, with micrometer sized crystals nucleating from the melt around these minerals, and along the margins of the melt with compositional zoning being present.

New crystal growth was abundant, observed having nucleated from the margins and within the center of the shock melt. Heterogenous nucleation of these crystals also occurred around the margins of host rock minerals entrained within the melt (Fig. 16d). The crystals nucleating within the center of the melt had a skeletal growth pattern (10 μm by 1 μm) with dark grey centers and brighter crystal rims, while the heterogenous nucleating crystals were more rectangular in shape with a less extreme change in grey-scale (Fig. 16c). EDX spot analysis of the crystals suggested a composition primarily of Mg-Fe silicates, often accompanied by minor Ca and Al. Raman analysis confirmed these compositions with two distinct spectral signatures consistent with olivine and pyroxene, respectively.

A complete summary of the optical deformation effects and high-pressure polymorphs present in the samples can be found in Table 4.

Discussion

The shock pressure-temperature-time constraints experienced by a meteorite may be estimated using high-pressure mineral states, solid-state transformations, the crystallization products of shock melt, and the shock deformation of host-rock minerals (Sharp and DeCarli 2007; Stöffler et al. 2018). The following discussion focuses on constraining the shock conditions of the meteorites in this study using the mineralogical, textural, and compositional observations reported in the results section. A summary of the constrained shock pressure estimates can be found in Table 5.

Overview of bulk shock in samples

Shock deformation effects in the crystalline igneous host rocks are consistent with moderate shock metamorphism. Pyroxene displays a combination of undulose extinction, polysynthetic mechanical twins, and weak mosaicism, while olivine exhibits minor planar fractures and weak to moderate mosaicism. The olivine and pyroxene phenocrysts are all colourless in plane polarized light and display maximum interference colours within the typical ranges for these minerals, suggesting shock discolouration has not occurred (Deer et al. 2013).

Based on the shock recovery experiments compiled by Stöffler et al. (2018), the deformation observed in mafic minerals in the meteorites in this study is consistent with shock pressures between 20 and 65 GPa. The lower limit of 20 GPa is constrained by the lack of undulatory extinction in olivine and the upper limit of 65 GPa bound by the presence of mosaicism and planar fractures in olivine (Fig. 17b).

Table 4. Shock Deformation and Transformations Observed in NWA 10597, NWA 8632, NWA 479, NWA 4898, and MIL 05035

Name	Planar Fractures	Undulose Extinction	Mosaicism	PDFs	Mineral Transformations
NWA 10597	2 orientations 20-30 um apart 2-3 um in width	Px	Ol	none	Maskelynite Coesite "Shocked" Tridymite
NWA 8632	2 orientations 20-100 um apart 2 um in width	Px	Px and Ol	none	Maskelynite
NWA 479	2 orientations 20-100 um apart 2 um in width	Px	Px and Ol	none	Maskelynite Ringwoodite
NWA 4898	n/a	none	Px and Ol	none	Maskelynite
MIL 05035	2 orientations 1-2 um apart less than 1 um width	Px	Px and Ol	none	Maskelynite Stishovite

Table 5. Constrained Bulk Shock Pressure Estimates for NWA 10597, NWA 8632, NWA 479, NWA 4898, and MIL 05035

NWA 10597		NWA 479		NWA 4898	
Previous Estimate	This Study	Previous Estimate	This Study	Previous Estimate	This Study
22-25 GPa	22-24 GPa	>23 Gpa	25-27 GPa	>9 Gpa	24-26 Gpa

NWA 8632		MIL 05035	
Previous Estimate	This Study	Previous Estimate	This Study
n.d	26-28 GPa	>25 Gpa	25-27 GPa

References for previous shock estimates are Chen et al. 2019 for NWA 10597, Miyahara et al. 2019 for NWA 479 and 4898, and Fernandes et al. 2010 for MIL 05035.
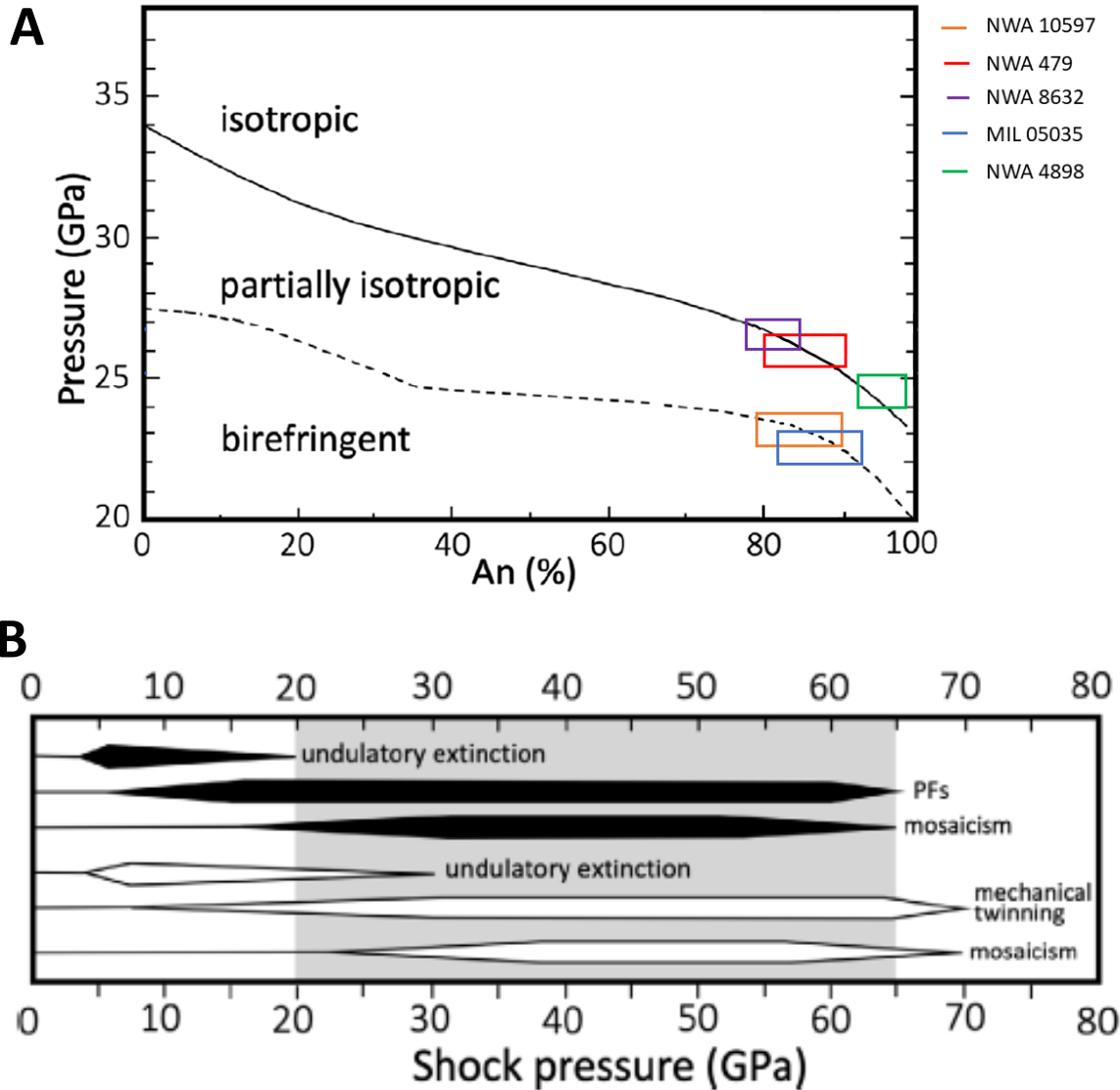
Fig. 17. A) A plot of the relationship between plagioclase composition and pressure based on curves in Fritz et al. (2019). The coloured boxes correspond to the compositional ranges of each sample with orange representing NWA 10597, Red representing NWA 479, purple representing NWA 8632, blue corresponding to MIL 05035, and green illustrating NWA 4898. The boxes indicate at what pressure the composition interacts with either the isotropic or partially isotropic plagioclase within each respective sample. B) Figure adapted from Mijajlovic et al. (2020) based on the data presented in Stoffler et al. (2018) illustrating the range of shock pressures olivine (black) and pyroxene (white) experienced according to the deformation observed in this studies meteorite samples. The shaded region refers to the upper and lower boundary constrained by this deformation.

Shock pressures above 40 GPa are unlikely due to the lack of additional shock features observed in olivine. Shock effects above this pressure (40 GPa) typically include discolouration of the olivine to an orange-brown due to the shock-induced formation of metallic nanoparticles from disassociated iron particles (Van de Moortèle et al. 2007). Additionally, the Raman spectra of host-rock olivine phenocrysts is consistent with well-crystallized olivine, displaying sharp, distinct peaks at 820 and 850 cm^{-1} (Chopelas 1991; Kuebler et al. 2006) whereas strongly shocked olivine will display additional peaks near 670 and 750 cm^{-1} with a broadening of the peaks due to structural disordering (Van de Moortèle et al. 2007). Despite the wide range of shock pressures over which mosaicism in olivine occurs (15 – 65 GPa), as the shock pressure increases, so does the number of misoriented domains within the olivine (Hörz and Quaide 1973). Strongly shocked olivine at pressures ≥30 GPa, displaying strong mosaicism, will often be accompanied by planar deformation lamellae (Stöffler et al. 2018). Not only were these lamellae not observed in the samples in this study, but the domains of mosaicism within the olivine were large and therefore few, suggesting a lower shock metamorphism. As such, the upper boundary bulk shock pressure of all five samples can be constrained to 30 GPa. The following subsections examine the mineral deformation and transformation within similarly textured meteorites, and then focuses on the localized shock melt in the samples individually.

Constraining Shock Conditions of NWA 8632, NWA 479, NWA 4898 using deformation and transformation of pyroxene, plagioclase and olivine

The texture of the plagioclase in NWA 479, NWA 8632, and NWA 4898 is like that of NWA 032 in which the structural state of the plagioclase was difficult to assess due to its small size in the groundmass (Fagan et al. 2002; Mijajlovic et al. 2020). NWA 8632 was originally reported to lack plagioclase, as reported in the Meteoritical Bulletin entry for this meteorite (Ruzicka et al. 2017). However, the BSE images collected on the fine-grained igneous portion of this meteorite show smooth, dark, 10 μm long plumose plagioclase intergrown with pyroxene. The plagioclase grains were first identified using BSE imaging (Fig. 6a) in which they appeared to be homogeneous and smooth, lacking any of the irregular fractures present in other crystalline minerals such as pyroxene. The Raman spectra of these uniform plagioclase grains confirmed an amorphous structure consistent with shock amorphized plagioclase indicated by the broadened peaks centered around 500 and 1000 cm^{-1}. Our Raman spectra of the maskelynite was consistent with naturally produced (Fritz et al. 2005) and experimentally produced (Fritz et al. 2019; Pittarello et al. 2020) maskelynite spectra. This spectrum contrasts with well crystalline plagioclase, which has a distinct triplet between 484 and 560 cm^{-1} and a

sharp peak between 980 and 1000 cm^{-1} (Freeman et al. 2008). In addition to the Raman spectra, the BSE images of the grains show none of the typical features associated with melting such as vesicles or schlieren flow structures, suggesting a solid-state transformation mechanism. There are no additional shock deformation features associated with these plagioclase grains that would be expected from a well crystalline mineral, which would include planar fractures and planar deformation features, depending on the shock pressures experienced by the bulk rock (Stöffler et al. 2018). Additionally, NWA 4898 was identified to contain complete transformation of plagioclase to maskelynite upon its publication within the meteoritical bulletin (Connolly et al. 2008). Therefore, our observations for the three samples are consistent with complete maskelynization of plagioclase in NWA 4898, NWA 479 and NWA 8632.

The effect of shock on feldspar has been well studied and applied to shock classifications due to the widespread occurrence of this mineral in in various rock types (e.g., felsic-anorthositic-mafic) (Stöffler 1971; Dodd and Jarosewich 1979; Stöffler et al. 1991, 2018; Stöffler and Grieve 2007; Fritz et al. 2017). The pressure at which plagioclase becomes shock amorphized has been demonstrated to be highly dependent on chemical composition of the crystalline feldspar mineral. The calcium end member (anorthite, $CaAl_2Si_2O_8$) has a greater ratio of aluminum atoms than that of the sodic and alkali endmembers (orthoclase, $KAlSi_3O_8$; albite, $NaAlSi_3O_8$) resulting in a greater number of weak Al-O bonds (Gibbons and Ahrens 1977; Fritz et al. 2019). As a result, the higher the Ca content of the feldspar, the lower the shock pressure required for shock amorphization, either partial transformation or complete transformation. NWA 479 has been paired with NWA 032 containing the same mineral compositions; it has a plagioclase composition of 80-90% anorthite (bytownite; Fagan et. al 2002). Based on the recast electron microprobe data (Table 3), the shock amorphized plagioclase observed in NWA 8632 has a 77-83% anorthite composition, slightly less calcic than its paired stones and therefore required higher shock pressures of 26 – 28 GPa to completely transform to maskelynite. Bytownite composition requires a minimum shock pressure of 25 – 27 GPa to completely transform to maskelynite, while the more calcic plagioclase composition in NWA 4898 require a lower minimum shock pressure of 24 – 26 GPa (Fig. 17a). The combined observations made of NWA 8632/479/4898 constrain a bulk shock pressure of <30 GPa with a lower boundary of 25 – 27 GPa for NWA 479, 26 – 28 for NWA 8632, and 26 – 28 GPa for NWA 4898/8632.

Constraining Shock Conditions of NWA 10597 using deformation and transformation of pyroxene, plagioclase and olivine

BSE imaging of plagioclase reveals a change in texture as the grains approach shock veins. At a distance from the vein, the plagioclase grains are highly fractured, and they become smoother and more homogeneous as the distance from the shock melt decreases (Fig. 6a). Raman spectra of these smooth, unfractured areas near the shock melt exhibit broadened peaks consistent with amorphous material. In contrast, the Raman spectra of the highly fractured areas at distance from the shock melt display a doublet peak at 469 cm^{-1} and 516 cm^{-1} with a strong peak at 1003 cm^{-1}. These amorphous areas near the shock melt combined with a crystalline structure elsewhere in the mineral confirm the partial maskelynization of plagioclase that had been previously observed in NWA 10597 (Chen et al. 2019). Partial maskelynization of plagioclase in shock veins has been reported in lunar meteorites, Martian meteorites, and terrestrial rocks (e.g., Walton et al. 2016; Sharp et al. 2019). The onset of maskelynization has been shown to be dependent on composition and temperature (Rubin 2015). Shock veins, which form from by friction and slip during shock compression, can generate heat with temperatures in excess of 2000 K which is then cooled by the conduction of the heat to surrounding host rock, resulting in feldspar grains that are in contact with the shock vein to experience higher temperatures compared to those of the host rock (Tomioka et al. 2010). It is the high temperatures surrounding the shock melt that lower the shock pressures required for the transformation to maskelynite resulting in partial maskelynization. Minerals along shock vein margins are also subjected to non-hydrostatic (shear) pressures, which lowers the shock pressures required for the onset of maskelynite (Daniel et al. 1997). The Raman spectrum of the crystalline plagioclase in NWA 10597 is consistent with a composition of bytownite (Freeman et al. 2018) which agrees with the mineral composition of An$_{78.5-88.7}$ originally reported (Bouvier et al. 2017). The partial maskelynization combined with the high Ca-content of the plagioclase constrains the lower boundary of the shock pressure for this meteorite to be 22 – 24 GPa (Fig. 17a).

Constraining Shock Conditions of MIL 05035 using deformation and transformation of pyroxene, plagioclase and silica

Maskelynite forms upon compression of the shock wave (Daniel et al. 1997). In MIL 05035 we document open fractures radiating from the silica margin, cutting across neighbouring maskelynite. Since maskelynite forms during shock compression, this cross-cutting relationship suggests a change in

density of the silica during decompression. This inference is supported by the mottled texture of silica grains. Raman spectroscopy of the light grey regions suggests that within the amorphous silica glass are irregular crystals of stishovite, indicated by the distinct peak at 754 cm^{-1}. Stishovite crystallizes between 8 and 30 GPa (Kayama et al. 2018) which is consistent with the bulk shock pressure constrained for this meteorite in previous studies (Fernandes et al. 2010). The lack of the acicular crystal shape commonly associated with stishovite crystals suggests that the silica transformed through a solid-state process as opposed to crystallizing from a melt (Ohtani et al. 2011). Raman spectroscopy of the amorphous silica glass surrounding the stishovite crystals has the defect bands at 490 cm^{-1} and 602 cm^{-1} that suggest the glass formed due to shock densification (Okuno et al. 1999). However, Heili et al (2016) have suggested that these defect bands may be an indicator of local density within the glass, not bulk density, and is therefore not reliable for assessing shock densification of binary silica glasses. It is also possible that the bands may be more indicative of the temperature at which the melted silica is cooled to a glassy state - called the fictive temperature - which ranges from 900 to 1400°C (Heili et al. 2016). This interpretation is supported by the decrease in the extent of the stishovite inclusion texture as it approaches the shock melt within the meteorite. This area that would have been higher in temperature as it approached the shock melt, thereby inhibiting preservation of the high-pressure phase. The distance the stishovite occurs from the shock melt suggests the inclusions were formed when an attenuated wave compressed the silica glass. The stishovite would have formed at the elevated pressure and then began back transforming during decompression. Near the shock melt, the increased heat of the melt would have radiated into the surrounding rock, destroying the high-pressure phases present in the glass and resulting in a smaller number of inclusions. Increased heat from shock melt and higher shock pressures has been shown to destroy high-pressure phases that would otherwise be present (Hu and Sharp, 2022).

Similar to NWA 10597, plagioclase grains in MIL 05035 are partially maskelynized, apparent in cross polarized light. The birefringent islands observed within otherwise isotropic grains have a Raman spectrum characteristic of crystalline anorthitic feldspar while the spectrum associated with the surrounding isotropic material is consistent with maskelynite. The partial transformation combined with the high-Ca content (An_{83-92}) constrains the minimum shock pressure that MIL 05035 would have experienced to be 21 – 24 GPa (Fig. 17a), with the same upper boundary as NWA 8632, NWA 479, NWA 4898 and NWA 10597 (<30 GPa). This shock pressure range is further supported by the minerals crystallizing from the shock melt of the meteorite as well as the high-pressure silica polymorphs, coesite and stishovite, that were observed in NWA 10597 and MIL 05035, respectively.

Localized Shock Melt in NWA 8632, NWA 479, NWA 4898, NWA 10597 and MIL 05035

In addition to glassy flow textures, the former melt present in NWA 479, NWA 8632, and NWA 4898 is observed to contain micrometer-size minerals. These minerals are found along the margins of the shock melt and entrained minerals, as well as in the vein centers (Fig. 12; Fig. 15; Fig. 16). These crystals are interpreted to have crystallized from melt based on their grain shape and observed core-rim chemical zoning present in BSE images. The presence of these crystals is indicative of a M-S4 classification with a shock pressure range of 28 – 34 GPa, as lower shock levels would contain less melt and therefore no crystal nucleation (Stöffler et al. 2018). This classification is consistent with our bulk shock pressure estimates (minimum of 25- 27 GPa with a maximum of 30 GPa). Raman spectra of the minerals crystallized from the melt were exclusively olivine and pyroxenes with olivine containing a doublet with the first peak 820 cm^{-1} and 850 cm^{-1} and pyroxene containing a triplet at 323, 356, and 392 cm^{-1} and two distinct peaks at 664 and 1006 cm^{-1} (Fig. 11). These minerals crystallize at shock pressures less than 14 GPa (Herzberg and Zhang 1996).

The quenched products of shock melting are used to search for minerals stable at high pressures which occur almost exclusively adjacent to shock melt (Sharp and DeCarli 2007). The P-T stability of these minerals, determined from static experiments, constrains the crystallization pressure of the melt which is related to the shock pressure experienced by the bulk rock dependent on the cooling history of the melt and shock duration (Xie et al. 2006; Hu and Sharp 2022). The paired stones NWA 479 and NWA 032 have been documented to contain ringwoodite in some samples (Miyahara et al. 2019) and not in others (Mijajlovic et. al 2020) which is consistent with the observations made in this study.

The shock veins of NWA 479 contain entrained clasts of host-rock minerals embedded in glass. These clasts range in size from <1 to 10 μm and comprise olivine and pyroxene with rounded margins. The Raman spectra from the olivine clasts exhibit intense doublet peaks at 799 and 844 cm^{-1} characteristic of ringwoodite, the high-pressure olivine polymorph (Fig. 13). Ringwoodite in this sample is interpreted to have formed through a solid-state mechanism because the grain size is too large (5 μm) to have crystallized from the shock melt during the short impulses for which shock waves last (<100 ms). Ringwoodite crystallizing from the shock melt would be sub-micrometer in size, typically requiring transmission electron microscopy (TEM) imaging to resolve as opposed to being viewable in reflected light (Walton et al. 2014).

Typically, ringwoodite forms at pressures >40 GPa (Hu and Sharp 2022) but has been shown to exist in mineral assemblages with olivine + clinopyroxene to pressures as low as 25 GPa (Hu and Sharp 2022). Our upper boundary constraint in NWA 479 (<30 GPa, discussed in *Constraining Shock Conditions of NWA 8632, NWA 479, NWA 4898 using deformation and transformation of pyroxene, plagioclase and olivine*) is also consistent with the presence of ringwoodite. Between the bulk shock pressures of 15 – 30 GPa, the temperature of the host rock, known as the Hugoniot temperature, is less than 800 K which is low enough to act as heat sink for the areas of localized melt allowing them to quench rapidly, preserving the high-pressure phases (Hu and Sharp 2022). Pressures above 30 GPa would result in higher temperatures and the presence of other high-pressure phases. Between 25 and 35 GPa we would expect to see bridgmanite and magnesiowüstite as the dominant minerals to have formed from olivine, and above 40 GPa the high temperatures would destroy the mineral phases (Hu and Sharp 2022). Ringwoodite is not ubiquitous throughout the shock veins, nor are other high-pressure phases such as bridgmanite or magnesiowüstite. This observation is consistent with the lower shock pressure of 25 GPa inferred from a mineral assemblage including olivine and pyroxene. Furthermore, this is consistent with the sample experiencing an attenuated shock wave as opposed to being located within the isobaric zone of a shock wave. In the isobaric zone, the difference between the peak shock pressure wave and the release wave is nearly a constant equilibrium, whereas outside the isobaric zone an attenuated wave experiences an immediate decay in shock pressure prior to cooling allowing high-pressure minerals to invert to their ambient pressure polymorphs (Asimow 2015; Fritz et al. 2017).

Therefore, we can conclude that the presence of ringwoodite agrees with our estimated bulk shock pressure and that the location of the sample outside of the isobaric zone resulted in the back transformation of high-pressure phases to ambient pressure igneous minerals for NWA 8632, NWA 479, and NWA 4898.

The localized quenched melt of NWA 10597 has a predominantly glassy texture with some crystallization along the margins of the shock melt. This melting and crystallization are in agreement with the upper shock boundary set by the mosaicism in olivine of <30 GPa. Localized mixed melting with glassy and microcrystalline textures correlates to shock pressures of 28 – 34 GPa (Stoffler et al. 2018). Raman spectra of the microcrystals reveal olivine and pyroxene, a representative of which is presented in Fig. 11. Silica grains located near pockets of melt exhibit a distinctly mottled light-dark texture in BSE images, similar to the texture observed in MIL 05035 (Fig. 7b). The SiO_2 content of both the dark grey and light grey patterns were measured using EDX spot analyses with no appreciable difference in

composition. These areas also contain minor amounts of Al_2O_3 (<1.5 wt% oxide). EPMA WDS spot analysis corroborates no appreciable difference in composition (Table 1). The grey-scale difference observed in BSE images could instead be attributed to different densities of the same composition. The possibility for the same compositions to have differences in grey scale due to density was demonstrated in El Goresy et al. (2008) during analysis of seifertite and silica glass. Raman analysis of this texture in this study reveals four distinct spectra. The light grey areas are consistent with coesite, displaying sharp peaks at 174 cm^{-1}, 264 cm^{-1}, and 520 cm^{-1} (Fig. 8). The dark grey areas show three distinct spectra: The first displays a broad hump centered around 500 cm^{-1} with a small peak around 605 cm^{-1}, which is interpreted to be silica glass due to its lack of distinct peaks and broadness characteristic of amorphous material (Fritz et al. 2005). The other two spectra are similar, with slightly different shifts and peaks between them. The spectra in this study contains peaks at 200 cm^{-1}, and 409 cm^{-1} with a deep valley between them (Fig. 8). Chen et al. (2019) attributed this spectrum to "shocked tridymite" in which the disordering of the tridymite combines the weaker intensity peaks with that of broad peaks around 200 cm^{-1} and 400 cm^{-1}. A similar spectrum was observed with a higher shift and more peaks at 201 cm^{-1}, 317 cm^{-1}, 413 cm^{-1}, 508 cm^{-1}, and 617 cm^{-1} (Fig. 8). Cristobalite is the best fitting spectrum of the silica polymorph as it typically displays peaks at 114 cm^{-1}, 230 cm^{-1} and 420 cm^{-1} (Bates 1972). Both the shocked tridymite and the cristobalite were observed in Chen et al. (2019). Both cristobalite and tridymite are ambient pressure polymorphs of silica while coesite occurs at elevated pressures of 2 – 8 GPa (Kayama et al. 2018).

The texture associated with the shock melt in NWA 10597 suggests that the high-pressure silica phases formed during the peak shock pressure wave and began to back transform upon decompression, as the heat from the shock melt would have prevented rapid quench crystallization of the high-pressure polymorphs (Hu and Sharp 2022). Therefore, this texture suggests the sample was located outside the isobaric zone of the impact. We infer that the silica back transformed to cristobalite or tridymite with remnants of coesite present as inclusions within the grain. The formation of these polymorphs agrees with the estimated bulk shock pressure of 22 – 24 GPa with a maximum of <30 GPa and is consistent with the results found in other paired stones of NWA 032 (Mijajlovic et al, 2020; Chen et al, 2019).

The Raman spectra of the minerals crystallizing from the shock melt of MIL 05035 are consistent with that of olivine and pyroxene, both of which crystallize at pressures <14 GPa (Herzberg and Zhang 1996). As shock is a notoriously heterogeneous process and despite the lack of high-pressure igneous minerals in this sample, we do note that they may occur in other samples as well as launch paired

stones. If high-pressure minerals are found in other thin sections and samples of these meteorites, such observations would still be in agreement with our estimated bulk shock pressure. The lack of consistent crystallization of high-pressure polymorphs throughout the shock melt would suggest the minerals crystallized from the melt during shock pressure release via an attenuated shock wave, outside the isobaric pressure zone (Hu and Sharp 2022). Furthermore, a mineral assemblage of high-pressure shock induced mineral crystallization that includes olivine and pyroxene has been shown to exist up to pressures of 25 GPa (Hu and Sharp 2022).

Chapter Three

Implications

Thermal Modelling

A finite element heat transfer (FEHT) code from F-Chart Software was employed to constrain the cooling duration experienced by the individual meteorite samples during the shock pulse and subsequent decay. Shock vein cooling history is modelled as a one-dimensional function of starting temperature and vein thickness that calculates transient heat flow from the shock vein to the surrounding host rock:

$$\frac{\partial}{\partial x}\left(k\frac{\partial T}{\partial x}\right) + \frac{\partial}{\partial y}\left(k\frac{\partial T}{\partial y}\right) - \rho c\frac{\partial T}{\partial t} = 0$$

Where *x* and *y* are distances in two dimensions, T is temperature [K], *k* is thermal conductivity [Wm^{-1} K^{-1}], ρ is density [kgm^{-3}], *c* is heat capacity [kJkg^{-1} K^{-1}] and *t* is time [s]. The samples were modelled at the minimum peak shock pressures constrained in the discussion section of this paper being 25 GPa (NWA 8632, NWA 479, NWA 4898, MIL 05035) and 22 GPa (NWA 10597) as well as their localized shock pressures based on shock melt vein mineral assemblage (8 GPa, a minimum for MIL 05035 and maximum for NWA 10597; 14 GPa for NWA 8632, NWA 479, NWA 4898). NWA 032 was also modelled based on the work of Mijajlovic et al. (2020) at a peak shock pressure of 25 GPa and a localized shock pressure of 14 GPa. Mid-ocean ridge basalt (MORB) was used as analogous to lunar basalt for the parameters necessary to perform the modelling. The density of MORB at the respective pressures is 3800 kg m^{-3}, 3750 kg m^{-3}, 3300 kg m^{-3}, and 3500 kg m^{-3} (Hirose et al. 1999). Heat capacity is extrapolated from low-pressure data resulting in 609 – 1335 kJ kg^{-1} K^{-1}, 687 – 1507 kJ kg^{-1} K^{-1}, 816 – 1788 kJ kg^{-1} K^{-1}, and 881 – 1930 kJ kg^{-1} K^{-1} for 8 GPa, 14 GPa, 22 GPa, and 25 GPa, respectively, across a temperature range of 300 – 3000 K. The effect of pressure on the thermal conductivity of MORB was calculated using

the method from Sharp et al. (2019) in which k(P, T) = k (1 Bar, T) · e^{aP} where P is pressure in GPa and a is a fitting factor of 0.03, the value for calcic pyroxene acting as an approximation for calcic plagioclase (Wang et al., 2014). This gives thermal conductivity values of 3.23 – 1.81 W m^{-1} K^{-1}, 3.86 – 2.17 W m^{-1} K^{-1}, 4.91 – 2.75 W m^{-1} K^{-1}, and 5.37 – 3.01 W m^{-1} K^{-1} for the same temperature range and respective shock pressures listed for heat capacity. The bulk-rock temperatures for the surrounding host rock of the models were determined by the Hugoniot of Kinosaki basalt at pressures of 8 GPa, 14 GPa, 22 GPa, and 25 GPa, resulting in temperatures of 450 K, 600 K, 750 K, 800 K, respectively (Nakazawa et al. 1997). The liquidus of the melt at the respective pressures (From Nakazawa et al. (1997): 2100 K, 2400 K, 2500, 2650 K) was used to constrain a starting temperature for the shock melt, corresponding to 100 K higher than the liquidus. Finally, the solidus temperature was determined to be the point at which the shock melt crystallized the high-pressure polymorphs observed within the shock veins (From Nakazawa et al. (1997): 1900 K, 2250 K, 2400K, 2500 K). NWA 10597 and NWA 479 were both modelled as 40 μm veins. NWA 10597 was surrounded by 1.87 mm of host rock and NWA 479 only 0.5 mm of host rock. The same model was used for NWA 4898 and MIL 05035 as they were both 12 μm veins surrounded by 0.3 mm of host rock. NWA 032 was a much larger vein measuring 92 μm surrounded by 2.75mm of host rock. Veins less than 100 μm and isolated from the thermal haloes of other shock melt are recommended for thermal modelling (Sharp et al. 2018). Due to the volume of shock melt and similarity to NWA 479 and NWA 032, NWA 8632 was not modelled.

The results of the modelling are summarized in Table 6. At both peak bulk pressure and preserved localized pressure, the super liquidus temperature of NWA 10597 would have cooled to the solidus in 0.30 ms. NWA 479 had peak bulk pressure and preserved localized pressure cooling times of 0.58 ms and 0.54 ms respectively. The model for NWA 4898 and MIL 05035 had cooling times of 0.037 ms at peak bulk pressure and a localized cooling time of 0.03 ms. NWA 032, a substantially larger vein, had a peak shock pressure cooling time of 3.78 ms and a localized shock pressure cooling time of 3.31 ms.

Pressure-Temperature-Time History

The mineral assemblages within the shock veins of NWA 4898 and NWA 479 indicate a complete solidification of shock melt at pressures <14 GPa, indicated by the presence of low-pressure olivine and pyroxene, the solid-state transformation of ringwoodite, and lack of bridgmanite and magnesiowüstite.

Table 6. Shock Melt Cooling Time Estimates for NWA 10597, MIL 05035, NWA 4898, NWA 479, and NWA 032

Sample	Vein Width (µm)	Pressure GPa	Solidus (˚K)	Liquidus (˚K)	Cooling Time (ms)	Difference (ms)
NWA 10597 (Peak)	40	22	2400	2500	0.3	
NWA 10597 (Local)	40	8	1900	2100	0.3	0.3
MIL 05035 (Peak)	12	25	2500	2650	0.037	
MIL 05035 (Local)	12	14	2250	2400	0.03	0.007
NWA 4898 (Peak)	12	25	2500	2650	0.037	
NWA 4898 (Local)	12	14	2250	2400	0.03	0.007
NWA 479 (Peak)	40	25	2500	2650	0.58	
NWA 479 (Local)	40	14	2250	2400	0.54	0.04
NWA 032 (Peak)	92	25	2500	2650	3.78	
NWA 032 (Local)	92	14	2250	2400	3.31	0.47

The same is true for NWA 032 which has shock melt estimated to have crystallized at ~ 13 GPa (Mijajlovic et al. 2020). The mineral assemblages within the shock veins of NWA 10597 and MIL 05035 have similar low-pressure igneous minerals in addition to the high-pressure silica polymorphs suggesting crystallization of the shock melt occurred between 2 – 8 GPa for NWA 10597 and <8 GPa for MIL 05035. The high-pressure polymorphs of silica are present as remnants within silica glass, suggesting back-transformation had begun prior to cooling and so peak shock pressure for MIL 05035 was not preserved. These cooling patterns, typical of material located outside the isobaric zone of a shockwave, indicate a rapid decay of shock pressure near the meteorites *in situ* location during the impact. In order for shock pressures to be preserved within the shock veins of a meteorite, the shock pulse must be longer than the cooling time (Shaw and Walton 2013). A variety of factors can extend the cooling time of shock melt including the size of the vein, the volume of melt within the sample, and the location of the meteorite with respect to the impact (Shaw and Walton 2013; Hu and Sharp 2022). As a result, shock veins less than 100 µm in width and isolated from other instances of shock melt are recommended for modelling (Shaw and Walton 2013; Sharp et al. 2018). The large temperature gradient between the super liquidus melt temperature and the bulk host rock allows for rapid quenching of the shock melt through conduction resulting in the preservation of high-pressure polymorphs (Hu and Sharp 2022). However, large volumes of melt producing thermal haloes and thick vein widths have been shown to increase cooling time by conduction resulting in partially annealed samples (Shaw and Walton 2013; Sharp et al. 2018; Hu and Sharp 2022). Furthermore, outside of the isobaric zone shock melt is cooled through the combined effect of conduction and adiabatic cooling due to decompression (Fig. 18). Shock melt rapidly quenched through conduction at high pressures has a near vertical slope of cooling, with temperature dropping rapidly while shock pressure decays minimally (Fig. 18). The slope of decompression cooling in basalt material remains above the liquidus for the entirety of the pressure release of a shockwave, destroying any evidence of high-pressure minerals (Hu and Sharp 2022). Based on mineral assemblage and back-transformation, the basaltic meteorites of this study experienced cooling due to a combined effect of decompression and conduction (shown in the yellow dashed line in Fig. 18).

Shock pulses on larger bodies are considerably shorter than the shock pulses recorded on smaller bodies. Shock pulses on Mars have been determined to be as low as 1 – 10 ms while shock pulses in chondrites have been modelled to have lasted as long as 1s. These values result in decompression dominating the cooling path of large body samples and conduction being more successful in preserving high-pressure minerals on smaller, chondritic bodies (Shaw and Walton 2013).
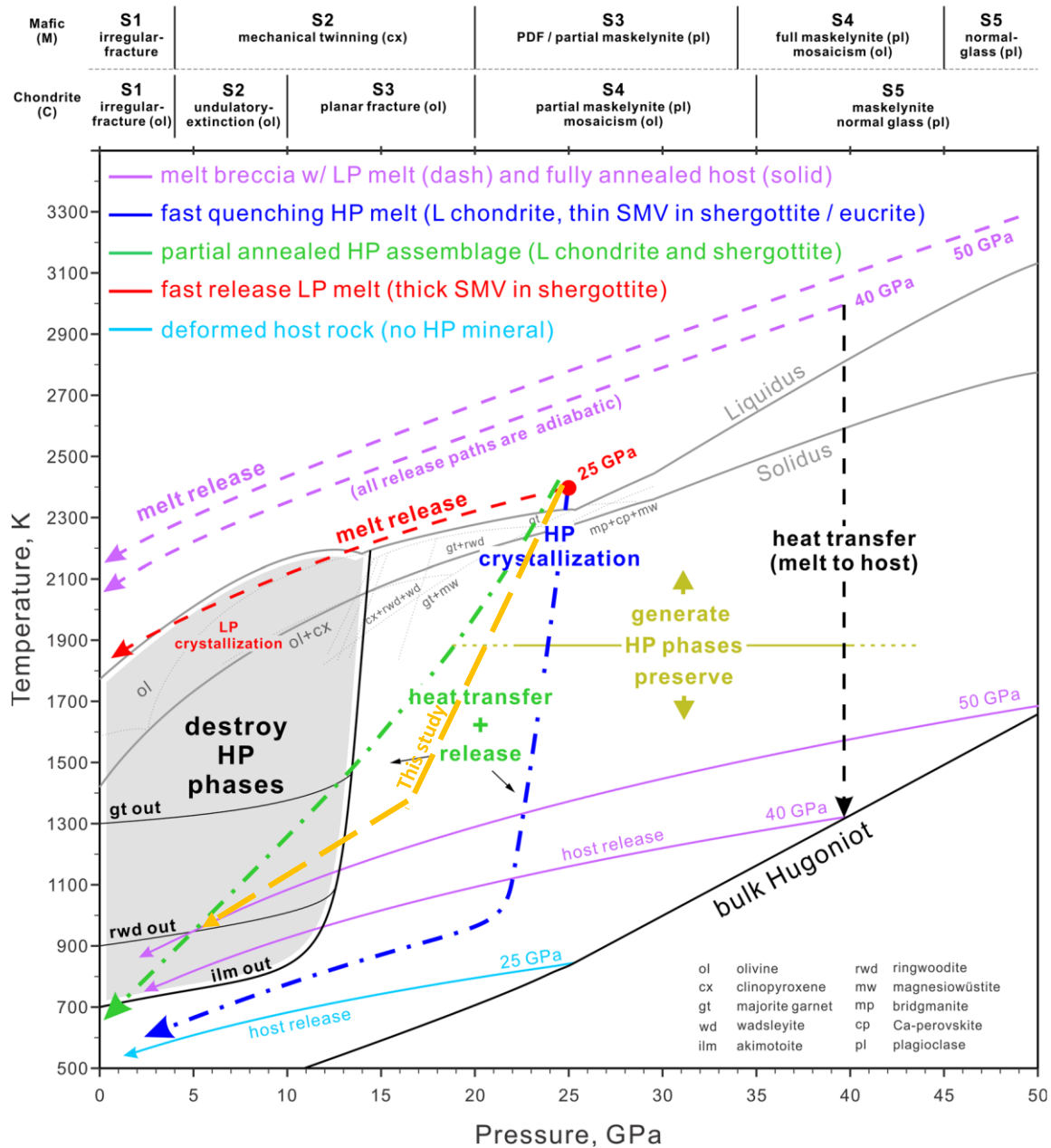
Fig. 18. Adapted from Hu and Sharp (2022) showing the different release paths a meteorite can take after cooling from a shock event. The blue HP crystallization line shows the slope of cooling for the preservation of high-pressure minerals while the green line shows the release path of samples that are partially annealed. Partially annealed samples are able to enter the destruction of high-pressure phases zone resulting in a lack of preservation of these phases. The cooling time of samples in this study is interpreted to be between the blue and green slopes (gold dashed line) based on the high-pressure minerals observed.

With the Moon being a body smaller than Mars, it is expected the duration of the shock pulse would be longer than 10 ms but shorter than 1s. As a result, the shock melt within our samples would require cooling times of less than 10 ms for the shortest shock pulse. However, the longest cooling time indicated by the FEHT modelling is 3.78 ms, well within the 10 ms time constraint - yet the minerals record shock pressures of <13 GPa. We interpret this as being due to the role decompression cooling plays in the mare basalts of this study. The FEHT models conduction cooling but does not take into account adiabatic release. Additionally, rapid pressure release results in highly vesiculated melt (Hu and Sharp 2022) which is a dominant texture within the shock melt of NWA 4898, NWA 8632, NWA 479, and NWA 032. The three latter samples also contain high volumes of melt with <1 mm of host rock on either side of the melt veins compared to previous models of Martian meteorites that contained shock veins surrounded by 9 mm of host rock (Sharp et al. 2019). The melt volume of these meteorites would have further contributed to the increased cooling time explaining the lack of high-pressure mineral preservation. However, small differences were apparent in the bulk peak-shock pressure and localized shock pressures of the samples such as in NWA 479, NWA 032, NWA 4898, and MIL 05035 (Table 6). We interpret these time differences to indicate the minimum amount of time required for the shock wave to decay to the localized pressure preserved within the veins, as cooling times were likely much longer than the model suggests. This is in agreement with the meteorites originating from outside the isobaric zones, as attenuated waves decay in shock pressure almost immediately.

Source Terranes and Pairing

The source-crater pairing and basalt flow pairing of a meteorite may be constrained using characteristics such as absolute age, crystal distribution, composition, cosmic-ray exposure ages, and REE abundances. The information provided by a suite of paired meteorites may then be capable of narrowing the origin point on the lunar surface when compared to a combination of remote sensing data, and samples returned from the Apollo and Luna missions. The ancient crystallization age (3.8 to 3.9 Ga), 2.0 wt% TiO_2, low Cr_2O_3, lack of KREEP components, high $^{147}Sm/^{144}Nd$ ratio, low $^{238}U/^{204}Pb$ ratio, and low $^{87}Rb/^{86}Sr$ ratio are the key components that Yamato-793169, Asuka-881757, MIL 05035, and MET 01210 (the "YAMM" suite of meteorites) have in common (Arai et al. 2010). The pairing of MET 01210 to the three basaltic meteorites in the YAMM suite provides sufficient context in which to identify the source terrane of these meteorites.

Unlike the basaltic meteorites it is paired with, MET 01210 has a unique mixing of mare to highland material occurring in a 68:32 ratio (Arai et al. 2010). This mixing combined with the ancient

crystallization age of the basalts suggests the origin of the YAMM meteorites is a cryptomare, a mare deposit subsequently covered by highland material (Arai et al. 2010). The geology, mineralogy, FeO-TiO$_2$-Th chemistry, basalt eruption age, and crater formation age of multiple cryptomaria have been well characterized through the Clementine Fe-Ti maps, Lunar prospector Th maps, and multispectral imaging. Using the same constraints that paired the YAMM meteorites, coupled with the mixing ratio of MET 01210, Arai et al. (2010) has suggested the origin of the meteorites to be a 1.4 km diameter crater within the Schickard Crater, located on the extreme SW limb of the lunar maria (48˚S and 50˚W). However, the methodology used to estimate source crater size is an inverse power law correlation between crater size and rate of crater formation (Warren 1994) that constrains the origin of the YAMM meteorites to the floor of Schickard Crater.

A similar approach has been undertaken using the LaPaz Icefield meteorite suite (02205/02224/0226/02436/03632/04841) which has been source-crater paired to NWA 032, NWA 10597, NWA 479, and NWA 8632 (Fagan et al. 2002; Zeigler et al. 2005; Anand et al. 2006; Day and Taylor 2007; Fernandes et al. 2009; Hill et al. 2009; Elardo et al. 2014; Chen et al. 2019) through bulk composition, mineralogy, and crystallization age indicating them to be different location samples of the same basaltic flow. Fernandes et al. (2009) used the age range of LAP 02205 acquired through Ar-Ar dating (2.985± 0.016 Ga and 3.15±0.07 Ga) to constrain two proximal melts within the Oceanus Procellarum that were of the appropriate age and provided a concordant elemental match. This suggests that the source-crater paired meteorites of NWA 032 originated from within the Oceanus Procellarum.

Unlike the other four samples in this study, NWA 4898 has a unique composition that has not been paired with any other known sample. It contains exceptionally low levels of TiO$_2$ but very high aluminum content of 12.4 wt% Al$_2$O$_3$ (Greshake et al. 2008). This composition is similar to Apollo 14 samples but lacks the KREEP components, suggesting it is from a currently unsampled lava flow and as a result has no paired meteorites or constrained source terrane (Li et al. 2016).

With the exception of the YAMM meteorite suite, which had unique evidence of cryptomare origin to help constrain a highly specific source region, the other meteorites in this study have at best been constrained to suspected basalt flows. In addition, YAMM meteorite crater size is based on statistics and not on the evidence provided by the meteorites themselves. The methodology of this study would use the shock effects in the meteorites coupled with thermal modelling to constrain a dwell

time that could be used to narrow down potential source crater diameters. Once possible source crater diameters are modelled, the measurements could be used to confirm the possibility of basalt flows as potential source candidates by searching for appropriately sized craters within the suggested areas. Such information could also be used to further support the potential source crater indicated in Arai et al. (2010) for the YAMM meteorites. The location of this study's meteorites outside the isobaric zone present significant challenges in establishing dwell time constraints due to the rapid decay of shock pressures resulting in partial annealing. As a result, the thermal modelling conducted in this study is only capable of constraining the minimum amount of time spent at peak shock pressure and as such, a minimum crater size with no limiting maximum. Despite this, the cooling rates of the single veins modelled in this study showed potential for constraining the shock decay rate based on the difference of cooling between peak pressure and the minimum pressure preserved in the shock veins based on the mineral assemblages that were present. The rate of decay could be further constrained if the cooling rates of a combination of high-pressure preserving shock veins were compared against each other. Due to the dependence of cooling rates on vein size, identifying the largest possible veins with the necessary mineral assemblages would help provide a better constraint of maximum cooling time. The suggested modelling approach would provide a more specific estimate of time spent at elevated pressures, similar to what was used to model crater diameters in Bowling et al. (2022). Additionally, a complete modelling of the full thin section taking into account the melt volume of the sample could better constrain the degree of adiabatic cooling and thermal haloes impacting the high-pressure mineral assemblage preservation.

Summary and Conclusions

Establishing the length of time a meteorite spent at elevated pressure is a key characteristic that allows for modelling the size of the source crater from which it originated. In order to establish dwell time, the pressure-temperature-time history of the meteorite must be interpreted and applied to thermal models. This study was able to tightly constrain the shock pressures experienced by the five samples, NWA 10597, NWA 8632, NWA 4898, NWA 479, and MIL 05035 to be used in conjunction with thermal modelling. NWA 10597 experienced bulk peak-shock pressures between 22 – 25 GPa, as indicated by the partial maskelynization of plagioclase feldspar within the host rock. Localized shock veins preserved a wide variety of shock densified quartz polymorphs, including coesite grains within silica glass that can be interpreted as back-transformation of high-pressure quartz polymorphs. NWA 479 and MIL 05035 all experienced shock pressures of 25 – 27 GPa while NWA 8632 likely experienced

shock pressures of 26 – 28 GPa, based on the composition of the plagioclase feldspar present in the meteorites and the degree of maskelynization (full vs. partial) observed. The shock veins within MIL 05035 preserve a similar mottled texture within silica glass to that of NWA 10597, with the preserved crystals being stishovite. Finally, NWA 4898, with a more anorthitic composition than the previous samples, likely experienced shock pressures from 24 – 26 GPa. All five samples were unlikely to have experienced bulk shock pressures beyond 30 GPa, constrained by the deformation of the minerals within the host rock. The cooling histories of the meteorites involved high temperatures during the shock event that lasted longer than the length of the shock wave pulse, allowing for the back transformation of high-pressure minerals to lower pressure polymorphs. Using what mineralogy was preserved within the shock veins, attempts were made to model the thermal history of the meteorites. While additional information and constraints would be necessary to establish a dwell time, the preliminary work done in this thesis demonstrates the possibility for establishing shock pressure decay rates for the samples and provides further support for the interpreted temperature-time histories of the meteorites. The large volume of melt within these samples presents challenges when differentiating between diabatic and adiabatic cooling during modelling; however, there is potential to overcome this through modelling the melt geometry of the entire thin section as opposed to singular shock veins. After obtaining this information, the terranes and basalt flows identified as potential source locations for these meteorites, can be investigated using modelled crater diameters. Source-crater diameters offer another parameter from which the exact location these samples originated from can be constrained, providing valuable and currently missing *in situ* context.

References

Ahrens, T. J., and O'Keefe, J. D. 1972. Shock melting and vaporization of lunar rocks and minerals. *Earth, Moon, and Planets: An International Journal of Solar System Science*. *4*:214–249.

Anand M., Taylor L. A., Floss C., Neal C. R., Terada K., and Tanikawa S. 2006. Petrology and geochemistry of LaPaz Icefield 02205: A new unique low-Ti mare-basalt meteorite. *Geochimica et Cosmochimica Acta*. 70:246–264.

Arai T., Hawke B., Giguere T., Misawa K., and Kojima H. 2010. Antarctic lunar meteorites Yamato-793169, Asuka-881757, MIL 05035, and MET 01210 (YAMM): Launch pairing and possible cryptomare origin. *Geochimica et Cosmochimica Acta* 74: 2231-2248.

Asimow P.D. 2015. Dynamic compression. In *Treatise on geophysics*, edited by Schubert G. Oxford: Elsevier. Pp. 393–416

Bates, J. B. 1972. Raman Spectra of α and β Cristobalite. *The Journal of Chemical Physics* 57:4042–4047.

Beck, P., Gillet, Ph., El Goresy, A., and Mostefaoui, S. 2005. Timescales of shock processes in chondritic and Martian meteorites. *Science* 435:1071–1074

Bischoff, A., and Stöffler, D. 1992. Shock metamorphism as a fundamental process in the evolution of planetary bodies: information from meteorites. *European Journal of Mineralogy*. 4:707–755.

Bouvier, A., Gattacceca, J., Grossman, J., and Metzler, K. 2017. The Meteoritical Bulletin, No. 105. *Meteoritics & Planetary Science*

Bowling, T. J., Johnson, B. C., Walton, E. L., Melosh, H. J., and Sharp, T. G. 2020. Dwell time at high

pressure of meteorites during impact ejection from Mars. *Icarus* 343: 113689.

Chen J., Jolliff B. L., Wang A., Korotev R. L., Wang K., Carpenter P. K., Chen H., Ling Z., Fu X., Ni Y., Cao H.,

and Huang Y. 2019. Petrogenesis and shock metamorphism of basaltic lunar meteorites

Northwest Africa 4734 and 10597. *Journal of Geophysical Research: Planets* 124:2583–2598.

Chopelas A. 1991. Single crystal Raman spectra of forsterite, fayalite and monticellite. *American

Mineralogist* 76:1101–1109.

Connolly H.C., Smith C., Benedix G., Folco L., Righter K., Zipfel J., Yamaguchi A., and Chennaoui

Aoudjehane H. C. 2007. The Meteoritical Bulletin, No. 92. *Meteoritics and Planetary Science*

42:1647–1694.

Connolly H.C., Smith C., Benedix G., Folco L., Righter K., Zipfel J., Yamaguchi A., and Chennaoui

Aoudjehane H. C. 2008. The Meteoritical Bulletin, No. 93. *Meteoritics and Planetary Science*

43:571–632.

Daniel I., Gillet P., McMillan P. F., Wolf G., and Verhelst M. A. 1997. High-pressure behavior of anorthite:

Compression and amorphization. *Journal of Geophysical Research: Solid Earth* **102**:313–325.

Day J. M. D., and Taylor L. A. 2007. On the structure of mare basalt lava flows from textural analysis of

the LaPaz Icefield and Northwest Africa 032 lunar meteorites. *Meteoritics & Planetary Science*

42:3–17.

Deer W. A., Howie R. A., and Zussman J. 2013. *An introduction to the rock-forming minerals*, 3rd ed.

London: The Mineralogical Society. 498 p.

Dence, M.R. 1965. The extraterrestrial origin of Canadian craters. *Annals of the New York Academy of Science* 123:941–969.

Dence, M.R. 1968. Shock zoning at Canadian craters: petrography and structural implications. In *Shock Metamorphism of Natural Materials,* edited by French B. M. and Short N.M. Baltimore, MD: Mono Book Corp. pp. 169–184.

Dodd R. T. and Jarosewich E. 1979. Incipient melting in and shock classification of L-group chondrites. *Earth and Planetary Science Letters* 44:335–340.

Elardo S. M., Shearer C. K., Fagan A. L., Borg L. E., Gaffney A. M., Burger P. V., Neal C. R., Fernandes V. A., and McCubbin F. M. 2014. The origin of young mare basalts inferred from lunar meteorites Northwest Africa 4734, 032 and LaPaz Icefield 02205. *Meteoritics & Planetary Science* 49:261–291.

El Goresy A., Dera P., Sharp T. G., Prewitt C. T., Chen M., Dubrovinsky L., Wopenka B., Boctor N. Z., and Hemley R. J. 2008. Seifertite, a dense orthorhombic polymorph of silica from the Martian meteorites Shergotty and Zagami. *European Journal of Mineralogy* 20:523–528.

Fagan T. J., Taylor G. J., Keil K., Bunch T., Wittke J. H., Korotev R. L., Jolliff B. L., Gillis J. J., Haskin L. A., Jarosewich E., Clayton R. N., Mayedda T. K., Fernandes V. A., Burgess R., Turner G., Eugster O., and Lorenzetti S. 2002. Northwest Africa 032: Product of lunar volcanism. *Meteoritics & Planetary Science* 37:371–94.

Fernandes V. A. S. M., Fritz J., Wünnemann K., and Hornemann U. 2010. K-Ar ages and shock effects in lunar meteorites (abstract). EPSC2010-237.

Freeman J. J., Wang A., Kuebler K. E., Jolliff B. L., and Haskin L. A. 2008. Characterization of natural feldspars by Raman spectroscopy for future planetary exploration. *The Canadian Mineralogist* 46:1477–1500.

French, B.M. 1998. Traces of a Catastrophe: A Handbook of Shock Metamorphic Effects in Terrestrial Meteorite Impact Structures (abstract). LPI Contribution No. 954. Houston, TX: Lunar and Planetary Institute.

French, B.M., and Short, N.M. 1968. Shock Metamorphism of Natural Materials. Baltimore, MD: Mono Book Corp.

Fritz, J., and Greshake, A. 2009. High-pressure phases in ultramafic rock from Mars. *Earth and Planetary Science Letters* 288:619–623.

Fritz J., Greshake A., and Stöffler D. 2005. Micro-Raman spectroscopy of plagioclase and maskelynite in Martian meteorites: Evidence of progressive shock metamorphism. *Antarctic Meteorite Research* 18:96–116.

Fritz J., Fernandes V. A., Greshake A., Holzwarth A., and Böttger U. 2019. On the formation of diaplectic glass: Shock and thermal experiments with plagioclase of different chemical compositions. *Meteoritics & Planetary Science* 54:1533–1547.

Fritz J., Greshake A., and Fernandes V. A. S. M. 2017. Revisiting the shock classification of meteorites. *Meteoritics & Planetary Science* 52:1216–1232.

Gibbons R. V. and Ahrens T. J. 1977. Effects of shock pressure on calcic plagioclase. *Physics and Chemistry of Minerals* 1:95–107.

Gladman B. J., Burns J. A., Duncan M. J., and Levison H. F. 1995. The dynamical evolution of lunar impact

ejecta. *Icarus* 118:302–321.

Greshake A., Irving A. J., Kuehner S. M., Korotev R. L., Gellissen M., and Palme H. 2008. Northwest Africa

4898: A new high-alumina mare basalt from the Moon. *Lunar and Planetary Science XXXIX*,

abstract no. 1631.

Grossman J. N., and Zipfel J. 2001. The Meteoritical Bulletin, No. 85. *Meteoritics & Planetary Science*.

Heili, M., Poumellec, B., Burov, E., Gonnet, C., Le Losq, C., Neuville, D. R., and Lancry, M. 2016. The

dependence of Raman defect bands in silica glasses on densification revisited. *Journal of*

Materials Science 51:1659–1666.

Herzberg C., and Zhang J. 1996. Melting experiments on anhydrous peridotite KLB-1: compositions of

magmas in the upper mantle and transition zone. *Journal of Geophysical Research* 101:8271–

8295.

Hiesinger H., Jaumann R., Neukum G., and Head, J. W. 2000. Ages of mare basalts on the lunar nearside.

Journal of Geophysical Research: Planets 105*:*29239–29275.

Hiesinger H., Head J.W., Wolf U., Jaumann R., and Neukum G. 2003. Ages and stratigraphy of mare

basalts in Oceanus Procellarum, Mare Nubium, Mare Cognitum, and Mare Insularum. *Journal of*

Geophysical Research: Planets 108:1-1– 1-27.

Hill E., Taylor L. A., Floss C., and Liu Y. 2009. Lunar meteorite LaPaz Icefield 04841: Petrology, texture,

and impact-shock effects of a low-Ti mare basalt. *Meteoritics & Planetary Science* 44:87-94.

Hirose K., Fei Y., Ma Y. and Mao H. K. 1999. The fate of subducted basaltic crust in the Earth's lower

mantle. *Nature* 397:53–56.

Hörz F., and Quaide W. L. 1973. Debye-Scherrer investigations of experimentally shocked silicates. *The*

Moon 6:45–82.

Hu, J., and Sharp, T. G. 2022. Formation, preservation and extinction of high-pressure minerals in
    meteorites: Temperature effects in shock metamorphism and shock classification. *Progress in
    Earth and Planetary Science 9*:6.

Joy K. H. and Arai T. 2013. Lunar meteorites: new insights into the geological history of the Moon.
    Astronomy & Geophysics 54:4.

Kayama, M., Nagaoka, H., and Niihara, T. 2018. Lunar and Martian Silica. *Minerals 8*:267.

Kenkmann T., Hornemann U., and St¨offler D. 2000. Experimental generation of shock-induced
    pseudotachylites along lithological interfaces. *Meteoritics & Planetary Science* 35:1275–1290.

Korotev R. L., and Irving A. J. 2021. Lunar meteorites from northern Africa. *Meteoritics & Planetary
    Science* 206–240.

Korotev, R. L. 2005. Lunar geochemistry as told by lunar meteorites. *Geochemistry* 65:297–346.

Kuebler K. E., Jolliff B., Wang A., and Haskin L. A. 2006. Extracting olivine Fo-Fa compositions from
    Raman spectral peak positions. *Geochimica et Cosmochimica Acta* 70:6201–6222.

Langenhorst, F. 2002. Shock metamorphism of some minerals: basic introduction and microstructural
    observations. *Bulletin of the Czech Geological Survey* 77:265–282.

Li S., Hsu W., Guan Y., Wang L., and Wang Y. 2016. Petrogenesis of the Northwest Africa 4898 high-Al
    mare basalt. *Meteoritics & Planetary Science* 51:1268-1288.

Melosh H. J. 1985. Ejection of rock fragments from planetary bodies. *Geology* 13:144–148.

Melosh, H.J., 1989. Impact Cratering: A geologic process. New York: Oxford Univ. Press.

Melosh, H. J. 2011. Planetary Surface Processes. Cambridge University Press.

Mijajlovic T., Xie X. and Walton E. L. 2020. A revised shock history for the youngest unbrecciated lunar basalt—Northwest Africa 032 and paired meteorites. *Meteoritics & Planetary Science* 55: 2267–2286.

Miyahara M., Kozuma K., Ohtani E., Yamaguchi A., Sakai T., Ohfuji H., Tomioka N., and Kodama Y.2019. Shock induced melting and high-pressure polymorphs in lunar basaltic meteorites (abstract #6014). LPI Contribution No. 2157. 82nd Annual Meeting of the Meteoritical Society.

Nakazawa S., Watanabe S., Kato M., Iijima Y., Kobayashi T., and Sekine T. 1997. Hugoniot equation of state of basalt. *Planetary and Space Science* 45:1489–1492.

Oberbeck, V.R. (1975) The role of ballistic erosion and sedimentation in lunar stratigraphy. *Reviews of Geophysics and Space Physics* 13: 337–362.

Ohtani, E., Ozawa, S., Miyahara, M., Ito, Y., Mikouchi, T., Kimura, M., Arai, T., Sato, K., Hiraga, K. 2011. Coesite and stishovite in a shocked lunar meteorite, Asuka-881757, and impact events in lunar surface. *Proceedings of the National Academy of Sciences* 108:463–466.

O'Keefe, J. D., and Ahrens, T. J. 1982. Impact mechanics of the Cretaceous–Tertiary extinction bolide. *Nature 298:*123–127.

Okuno M., Reynard B., Shimada Y., Syono Y., and Willaime C. 1998. A Raman spectroscopic study of shock-wave densification of vitreous silica. *Physics and Chemistry of Minerals* 26:304-311.

Osinski, G. R., and Pierazzo, E. 2013. *Impact cratering: Processes and products*. Hoboken, NJ: Wiley-Blackwell. pp. 1 – 17.

Pasek, M. A. 2017. Schreibersite on the early Earth: Scenarios for prebiotic phosphorylation. *Geoscience Frontiers* 8:329–335.

Pike, R.J. 1980. Control of crater morphology by gravity and target type – Mars, Earth, Moon. *Proceedings of the Lunar and Planetary Science Conference* 11:2159–2189.

Pittarello L., Fritz J., Roszjar J., Lenz C., Chanmuang N. C., and Koeberl C. 2020. Partial amorphization of experimentally shocked plagioclase: A spectroscopic study. *Meteoritics & Planetary Science* 55:669–678.

Rubin A. E. 2015. Maskelynite in asteroidal, lunar and planetary basaltic meteorites: An indicator of shock pressure during impact ejection from their parent bodies. *Icarus* 257:221–29.

Ruzicka A., Grossman J. N., Bouvier A., and Agee C. B. 2014. The Meteoritical Bulletin, No. 103. *Meteoritics & Planetary Science* 36:A293-A322.

Rubin, A.E., Scott, E.R.D. and Keil, K. 1997. Shock metamorphism of enstatite chondrites. *Geochemica et Cosmochimica Acta* 61:847–858.

Sharp T. G. and DeCarli P. S. 2007. Shock effects in meteorites. In *Meteorites and the early solar system II*, edited by Lauretta D. S. and McSween H. Y. Jr. Tucson, Arizona: The University Press. pp. 653–678.

Sharp, T.G., Walton, E.L., Hu, J., 2019. Shock conditions recorded in NWA 8159 Martian augite basalt with implications for the impact cratering history of Mars. *Geochimica et Cosmochimica Acta* 246:197–212.

Shaw C. S. J., and Walton E. L. 2013. Thermal modeling of shock melts in martian meteorites:

implications for preserving martian atmospheric signatures and crystallization of high-pressure

minerals from shock melts. *Meteoritics & Planetary Science* 48:758–770.

Shoemaker, E.M. 1960. Penetration mechanics of high velocity meteorites, illustrated by Meteor Crater,

Arizona, in *Report of the International Geological Congress*, XXI Session, Norden. Part XVIII,

International Geological Congress, Copenhagen, pp. 418–434.

Stöffler D. 1971. Progressive shock metamorphism and classification of shocked and brecciated

crystalline rocks at impact craters. *Journal of Geophysical Research* 76:5541–5551.

Stöffler D. and Grieve R. A. F. 2007. Impactites. *In Metamorphic rocks: A classification and glossary of

terms, recommendations of the International Union of Geological Sciences*., edited by Fettes D.

and Desmons J. Cambridge: Cambridge University Press. pp. 82–91, 111–125, and 126–242.

Stöffler D., Keil K., and Scott E. R. D. 1991. Shock metamorphism of ordinary chondrites. *Geochimica et

Cosmochimica Acta* 55:3845–3867.

Stöffler, D., and Langenhorst, F. 1994. Shock metamorphism of quartz in nature and experiment: I. Basic

observation and theory. *Meteoritics and Planetary Science* 29:155–181.

Stöffler D., Ryder G., Ivanov B. A., Artemieva N., Cintala M. J., and Grieve R. A. F. 2006. Cratering history

and lunar chronology. In *New views of the Moon*, edited by Jolliff B. L.

Stöffler D., Hamann C., and Metzler K. 2018. Shock metamorphism of planetary silicate rocks and

sediments: Proposal for an updated classification system. *Meteoritics & Planetary Science* 53:5–

49.

Taylor G.J. 2009. Ancient lunar crust: origin, composition, and implications. *Elements* 5:17–22.

Tomioka N., Kondo H., Kunikata A., and Nagai T. 2010. Pressure-induced amorphization of albitic

plagioclase in an externally heated diamond anvil cell. *Geophysical Research Letters* 37:L21301.

Van de Moortèle B., Reynard B., McMillan P. F., Wilson M., Beck P., Gillet P., and Jahn S. 2007b. Shock-

induced transformation of olivine to a new metastable (Mg, Fe)2SiO4 polymorph in Martian

meteorites. *Earth & Planetary Science Letters* 261:469–475.

Vaniman D., Dietrich J., Taylor G. J., Heiken G.1991.Exploration, samples, and recent concepts of the

Moon. In: *The lunar sourcebook: a user's guide to the Moon,* edited by Heiken G. H., Vaniman D.,

French B. M. Cambridge University Press, New York, pp 5–26.

Walton E. L., Sharp T. G., and Hu J. 2016. Frictional melting processes and the generation of shock veins

in terrestrial impact structures: Evidence from the Steen River impact structure, Alberta,

Canada. *Geochimica et Cosmochimica Acta* 18:256–270.

Walton E. L., Sharp T. G., Hu J., and Filiberto J. 2014. Heterogeneous mineral assemblages in Martian

meteorite Tissint as a result of a recent small impact on Mars. *Geochimica et Cosmochimica Acta*

140:334–348.

Wang C., Yoneda A., Osako M., Ito E., Yoshino T., and Jin Z. 2014. Measurement of thermal conductivity

of omphacite, jadeite, and diopside up to 14 GPa and 1000 K: implication for the role of eclogite

in subduction slab. *Journal of Geophysical Research: Solid Earth* 119:6277–6287.

Warren, P. H., and Kallemeyn, G. W. 1991. Geochemical investigation of five lunar meteorites:

Implications for the composition, origin and evolution of the lunar crust. *Proceedings of the NIPR*

Symposium on Antarctic Meteorites 4:91 – 117.

Warren P.H., and Taylor G.J. 2014. The Moon. In *Treatise on Geochemistry,* edited by Holland H. D. and

Turekian K. K. Elsevier Ltd. pp. 213 – 244.

Xie Z., Sharp T. G., and DeCarli P. S. 2006. High pressure phases in a shock-induced melt vein of the

Tenham L6 chondrite: Constraints on shock pressure and duration. *Geochimica et Cosmochimica*

Acta 70:504–515.

Zeigler, R. A., Korotev, R. L., Jolliff, B. L., and Haskin, L. A. 2005. Petrography and geochemistry of the

LaPaz Icefield basaltic lunar meteorite and source crater pairing with Northwest Africa 032.

Meteoritics & Planetary Science 40:1073–1101.